Rapport de la réunion d'automne de la SSP

Autor(en): **[s.n.]**

Objekttyp: **AssociationNews**

Zeitschrift: **Helvetica Physica Acta**

Band (Jahr): **66 (1993)**

Heft 1

PDF erstellt am: **09.08.2024**

Nutzungsbedingungen

Die ETH-Bibliothek ist Anbieterin der digitalisierten Zeitschriften. Sie besitzt keine Urheberrechte an den Inhalten der Zeitschriften. Die Rechte liegen in der Regel bei den Herausgebern.
Die auf der Plattform e-periodica veröffentlichten Dokumente stehen für nicht-kommerzielle Zwecke in Lehre und Forschung sowie für die private Nutzung frei zur Verfügung. Einzelne Dateien oder Ausdrucke aus diesem Angebot können zusammen mit diesen Nutzungsbedingungen und den korrekten Herkunftsbezeichnungen weitergegeben werden.
Das Veröffentlichen von Bildern in Print- und Online-Publikationen ist nur mit vorheriger Genehmigung der Rechteinhaber erlaubt. Die systematische Speicherung von Teilen des elektronischen Angebots auf anderen Servern bedarf ebenfalls des schriftlichen Einverständnisses der Rechteinhaber.

Haftungsausschluss

Alle Angaben erfolgen ohne Gewähr für Vollständigkeit oder Richtigkeit. Es wird keine Haftung übernommen für Schäden durch die Verwendung von Informationen aus diesem Online-Angebot oder durch das Fehlen von Informationen. Dies gilt auch für Inhalte Dritter, die über dieses Angebot zugänglich sind.

Ein Dienst der *ETH-Bibliothek*
ETH Zürich, Rämistrasse 101, 8092 Zürich, Schweiz, www.library.ethz.ch

http://www.e-periodica.ch

Helv Phys Acta
Vol. 66 (1993)

0018-0238/93/010053-52$1.50+0.20/0

Restoration of Scanning Tunneling Images Distorted by Time-Dependent Effects of the Piezo Driver and the Nonlinear Feedback System

E. P. Stoll

IBM Research Division, Zurich Research Laboratory, 8803 Rüschlikon

The distortions of scanning tunneling microscope images due to time-dependent effects can be eliminated by correcting for piezo after-effects assuming a logarithmic time dependence in the scan direction and applying a nonlinear feedback simulation model to correct for tip height deviations.

STM images are often adversely affected by geometrical distortions due to time-dependent after-effects in the piezo drivers [1]. These distortions are primarily visible at the boundaries where the scans begin or where the direction of the tip motion is reversed. In the conventional constant current mode the feedback system [2] increases or decreases the voltage applied to the z-piezo, thus moving the tip perpendicular to the measured sample surface until the current reaches a preset value. Because this voltage is recorded and displayed in the images, the above-mentioned after-effects give rise to overshooting at steps. Furthermore, the feedback is unable to follow the sample surface profile if very abrupt or short-wavelength height changes occur. The resulting artifacts are different for upward and downward motion and can be made visible by comparing adjacent forward and backward scans simultaneously. Such artifacts can be eliminated by correcting for piezo after-effects assuming a logarithmic time dependence in the scan direction and applying a nonlinear feedback simulation model to correct for tip height deviations.

Within the context of STM the first quantitative description of long time-dependent after-effects in piezo-ceramic rods commonly used for drivers was made by Vieira [1]. For scans recorded with a constant velocity, the following relation between the actual coordinate x of the scanned surface and that of the recorded picture holds according to Ref. 3

$$x' = x(1 + \alpha \ln x/x_0) + \Delta x, \tag{1}$$

where α is a parameter describing creep processes, x_0 denotes the scan length and Δx is the scanned distance during the dead time between two recorded scans.

Assuming for simplicity a perfect (instantaneous) feedback response, the overshooting effect can be estimated by convoluting the second derivative of Eq. (1), a $1/x$-function, with the recorded scan function. This yields

$$z(x) = z'(x) + \beta \int z'(x') \frac{1}{x - x'} \, dx', \tag{2}$$

with β a fit parameter describing the relative extension of the x- and z-piezos, respectively.

Much more severe than this overshooting effect is the extent to which the recorded corrugation is perturbed by the latency of the feedback system. This latency depends on the sign and the magnitude of the surface height change

$$\frac{\partial z(x)}{\partial x} = \widetilde{N}(z_0(x - \Delta) - z(x - \Delta)), \tag{3}$$

where z_0 is the actual surface corrugation, Δ is the motion of the tip in the x-direction during the time lag of the feedback circuit and N is a nonlinear function. Inverting Eq. (3), we obtain

$$z_0(x-\Delta) = z(x-\Delta) + N\left(\frac{\partial z(x)}{\partial x}\right), \tag{4}$$

with $N(y)$ being the inverse of $\tilde{N}$. Here, for $y \equiv \partial z/\partial x > 0$ we found that N is well represented by the logarithm $(1/\eta \ln(\varepsilon\eta y + 1))$ and for $y < 0$ we can assume instead an exponential $(1/\eta[1 - \exp(-\varepsilon\eta y)])$. ε and η are the feedback and the nonlinearity parameters. Indeed, for $\varepsilon\eta y \ll 1$ we recover the usual linear dependence $N(y) \simeq \varepsilon y$.

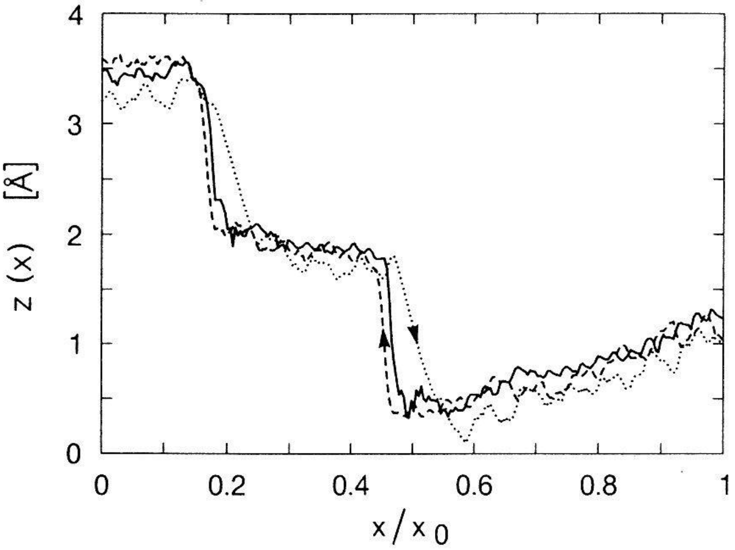

Figure 1: Two successive scans on a gold (110) surface from left to right (dotted) and right to left (dashed). The solid curve shows the corrected averaged scan with the parameters: $\alpha = 0.015$, $\beta = 0.01$, $\varepsilon = 1.35$, $\eta = 0.508$, $x_0 = 345$ Å, $\Delta x/x_0 = 0.004$ and $\Delta/x_0 = 0.00233$.

Figure 1 shows a scan from left to right (dotted) and one from right to left (dashed) on a gold (110) (2×1) surface [4] with two steps (see Ref. 5). The hysteresis and the feedback latencies are clearly visible. Furthermore this latency is more pronounced at downward than at upward steps. The parameters of Eqs. (1)-(4) are determined by maximizing the cross-correlation between the corrected scans from left to right and right to left.

With these procedures piezo after-effects and the feedback latency effects can be corrected. It should be noted however, that for the corrections in Eq. (4) the numerical differential $\partial z/\partial x$ should be taken from low-pass filtered recorded profiles $z(x)$ so that high-frequency contributions of the derivative are not too amplified.

I would like to thank A. Baratoff for careful proofreading of the text.

References

[1] S. Vieira, IBM J. Res. Develop. **30**, 553, (1986).
[2] O. Marti, *Scanning Tunneling Microscope at Low Temperatures*, Ph.D Thesis No. 8095, Swiss Federal Institute of Technology, ETH Zurich (1986).
[3] E.P. Stoll, Ultramicroscopy, **42-44**, 1585 (1992).
[4] R. Gaisch, J.K. Gimzewski, B. Reihl, R.R. Schlittler, W. Schneider, E. Stoll and M. Tschudy, unpublished results (1992).
[5] J.K. Gimzewski, R. Berndt and R.R. Schlittler, Phys. Rev. B **45**, 6844 (1992).

Domain Wall in Thin Films of Ferroelectric BZT

M. Robert[1], I. Reaney[2] and P. Stadelmann[3]

1 Rice Quantum Institute, Rice University, Houston, Texas 77251-1892, USA; on leave at Institut Interdépartemental de Microscopie Electronique, EPFL, CH-1015 Lausanne, Switzerland;
2 Laboratoire des Céramiques, Département des Matériaux, EPFL, CH-1015 Lausanne, Switzerland;
3 Institut Interdépartemental de Microscopie Electronique, EPFL, CH-1015 Lausanne, Switzerland;

Transmission electron microscopy is used to study the structure of the domain wall in thin films of ferroelectric BZT (barium zirconium titanate $BaZr_xTi_{1-x}O_3$), as a function of temperature from room temperature to that of the Curie point, which is a critical point at which the thickness of the domain wall diverges.

When two phases coexist at equilibrium, they are separated by an interface across which the physical properties change continuously from those of one phase to those of the other. Far from a critical point, the thickness of the interface is typically a few angströms, but as a critical point is approached, it increases considerably, ultimately diverging at the critical point itself.

Recently, it has been shown [1] that close to a critical point, the behavior of interfaces of two-dimensional systems differs drastically from that of three-dimensional systems; in particular, it has been shown [2] that, unlike in three or more dimensions of space, the critical exponent describing the divergence of the interfacial thickness at a critical point is a nonuniversal function of the external field, in contrast to the commonly accepted view that in the critical region, the interfacial thickness is proportional to the correlation length of the spontaneous fluctuations in the coexisting bulk phases. Unfortunately, the only experimental results available concern fluids in three dimensions.

Here, we present the first results for a thin film of a ferroelectric material exhibiting a second-order phase transition [3], i.e., for which the Curie point is a critical point. The experimental method used in that of Transmission Electron Microscopy, which had already been successfully used by one of us [4] to study the interfacial structure of the ferroelectric $PbTiO_3$. In that case, a high-resolution analysis showed that the thickness of the interface (domain wall) at room temperature, which is far from that of the Curie point, is of the order of the lattice spacing. Because $PbTiO_3$, like most ferroelectrics, exhibits a first-order phase transition, the thickness of the domain wall does not diverge at the Curie point.

The material we study is BZT, barium zirconium titanate $BaZr_xTi_{1-x}O_3$, with $x= 0.13$.

The critical temperature of the bulk is T_c = 75°C. Thin foils of about 1500 Å were prepared from a ceramic. The samples were imaged in Bright Field using a Hitachi HF-2000 electron microscope operated at 200 kV.

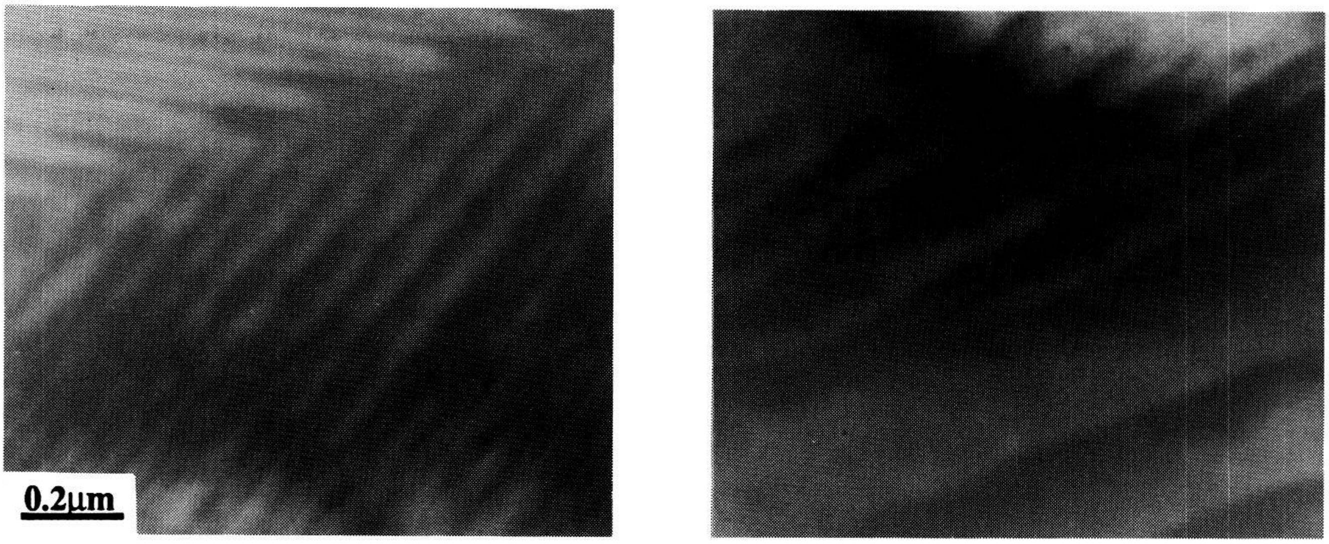

Figures 1: Domain walls at room temperature (left) and close to the Curie point (right).

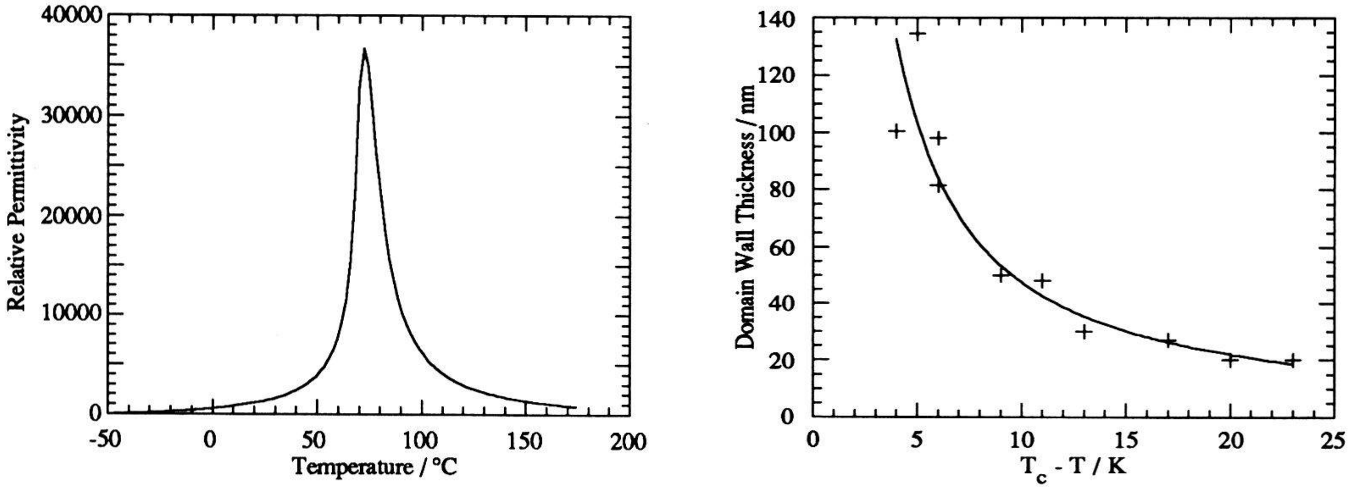

Figures 2: Plot of relative permittivity as a function of temperature showing a typical 2nd order phase transition in BZT (left) and the thickness of domain walls as a function of temperature in BZT (right).

The authors acknowledge Dr. A. Bell and O. Hunziker for preparing the BZT sample and Dr. A. Bell for fruitful discussions. This work was supported in part by the Welch Foundation (Houston, Texas).

[1] M. Robert, Phys. Rev. **A30**, 2785 (1984).
[2] M. Knackstedt and M. Robert, Int. J. Thermophysics **10**, 321 (1989).
[3] D. Hennings et al., J. Am. Ceram. Soc. **65**, No 11, 539 (1982).
[4] R. Spycher, P.A. Buffat and P. Stadelmann, Helv. Phys. Acta **60**, 804 (1987).

TIME RESOLVED PHOTOELECTRON SPECTROSCOPY DURING MICROSECOND LASER MELTING OF SURFACES

G. Gantner, P. Oelhafen, H.-G. Boyen and K. Rink*
Institut für Physik, Klingelbergstrasse 82, 4056 Basel, Switzerland.
*Centre d'application de laser, EPFL Lausanne, Switzerland.

A new method for performing photoelectron spectroscopy is presented. It offers in particular the possibility to investigate systems which up to now could not be measured because of their high vapor pressure. This is realized by µsec-laserpulse irradiation of the sample allowing the surface to heat up for a few microseconds and cool down to the initial temperature. The experimental setup and first results are presented.

Until now measurements of the electronic density of states (DOS) by photoelectron spectroscopy (PES) have been a invaluable for the understanding of properties of the crystalline, amorphous and liquid state. Especially the comparison of the DOS of atomically ordered with disordered phases has allowed an important insight into the interplay of the atomic and electronic structure [1,2], showing that the simple picture of the free electron model (FEM) behaviour for liquids is not correct.

Unfortunately, due to the elevated vapour pressure above the melting point, the major part of the elements cannot be measured by electron spectroscopy. The emitted electrons, excited by UV- (typ. HeI, hν = 21.2 eV) or X-ray- (e.g. Al Kα, hν = 1486.6 eV) photons, suffer secondary scattering from the vapour, losing their energy-information and the UHV- chamber may become contaminated. To extend PES also to these elements we are developing a new technique for measuring the liquid phase, based on pulsed heating of the sample surface.

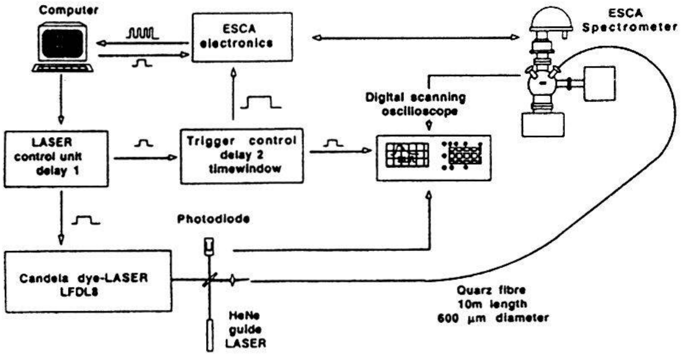

Fig.1: Experimental setup for PES during LASER pulse heating.

Figure 1 shows the experimental setup of the LASER pulse heating combined with modified conventional PES measuring system. A flashlamp-pumped dye-LASER of λ= 593 nm and FWHM = 2.5 µsec is used to heat up and melt the surface of the sample. While the surface is liquid, which is in the order of a few µsec, the ESCA electronic is enabled to count the electrons emitted continuously from the sample surface, taking into account the time of flight of the electrons between sample surface and detector. Since the electron-phonon relaxation time lies in the range of psecs [3], the energy absorbing electron system is in equilibrium with the phonon system and the sample is liquid in the conventional sense. On the other hand, however, the mean dwell time of a surface atom, i.e. the time a probe atom of the sample surface needs to overcome the surface potential and get into vacuum at a given temperature following an Arrhenius law, can be several microseconds. It is this delayed vapour emission which prevents the interaction with the photoelectrons which are emitted practically instantaneously. The released atoms moreover, having only thermal velocities, can be easily separated from the fast electrons with energies of several tens of eV, due to different time of flight. After each heat-up and cool- down cycle the electron-analyzer is set to the next energy channel and the whole measurement is repeated until the required quality of statistics is obtained.

Figure 2 shows first results for parts of the valence bands of Au and Ge we have obtained with this new method. Au and Ge could also be measured conventionally accepting a severe contamination of the chamber , X-ray source window etc. . The results obtained with the LASER pulse heating method are in good agreement with these results. Especially it can be seen easily from the Fermi-edge that Ge changes from a semiconductor to a metal by melting, which is a wellknown fact. The spectrum, taken by G. Indlekofer with the conventional method, does excellently fit the data of the LASER-heating method. The Au spectrum shows the typical shift of the d-band edge at 2.0 eV to lower binding energy, and a rounding of the d-peak due to the absence of direct transitions, both correlated with the rising temperature. During all these measurements no chamber contamination was detectable , although the samples were in a liquid state. The sample surfaces have been smoothed by the LASER, but not destroyed.

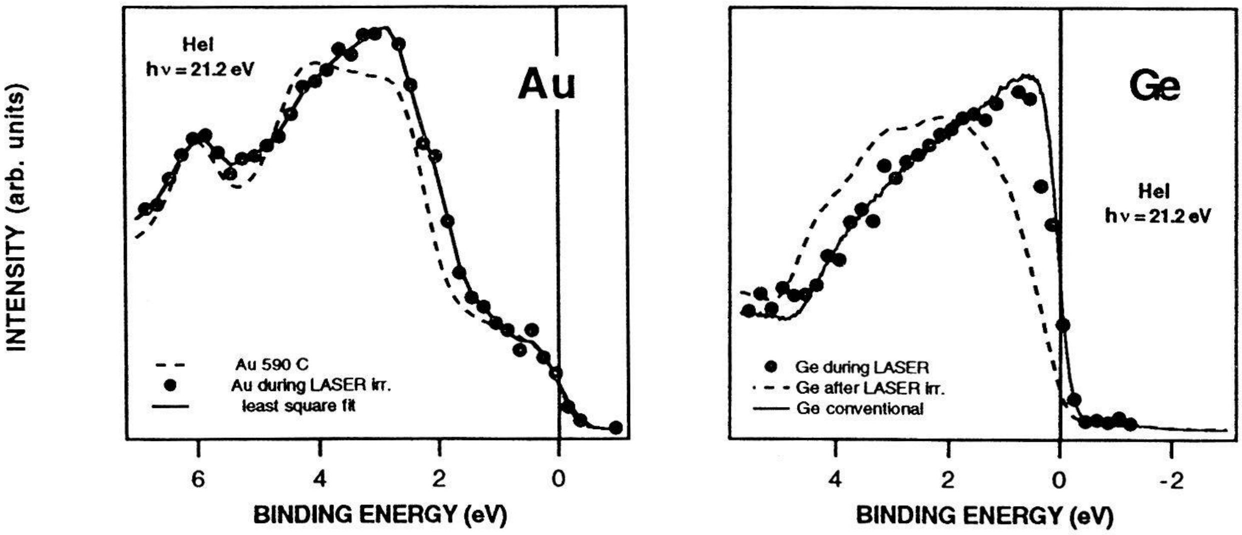

Fig.2: UPS spectra of Au and Ge taken during and after LASER irradiation.

In conclusion, we can say that this measurement technique is able to deliver spectra of elements in the liquid state, even if they have high vapour pressure. It will give access to the DOS of a wider variety of liquid elements than it has been possible up to now. With the improvements we have planned, it will even be possible to get a sequence of spectra monitoring the whole phase transition.

Acknowledgements: Financial support by the Swiss National Foundation is gratefully acknowledged.

References [1] W. Jank and J. Hafner, Phys.Rev. B **42,** 6926 (1990) and ref. therein.

[2] G. Indlekofer and P. Oelhafen, J. Non.-Cryst. Solids **117&118,** 340 (1990)

[3] H.E. Elsayed-Ali et al. Phys. Rev. Letters **58** (12), 1212 (1987)

Photoemission study of the diamond/silicon interface and surface evolution of diamond grown on Si(100) by microwave plasma CVD

G. Francz, P. Kania, P. Oelhafen
Institut für Physik der Universität Basel, Klingelbergstrasse 82, CH-4056 Basel

Photoelectron techniques were used to study the different phases in the initial growth of polycrystalline diamond on Si(100) substrates. Diamond films were deposited by microwave assisted chemical vapor deposition from a CH_4/H_2 mixture. The surface compositions of the as grown films were probed in function of deposition time. The XPS data reveals the formation of a SiC phase at the early stage of nucleation, preceeding the gradual growth of diamond. At intermediate stages a combination of different carbon phases (namely SiC and diamond) was observed depending on experimental conditions.

Introduction Nucleation of diamond and the resulting interface between a diamond film and a non-diamond substrate are critical phenomena which has profound influence on the subsequent growth of the film. Despite of the great activity in the field of CVD diamond, a complete understanding of the interfacial structure, which is closely related to such important issues as epitaxial growth, nucleation, adhesion, and the control of optical as well electrical properties, still needs to be solved. In order to obtain more information about these problems, spectroscopies that can monitor changes which occur on the growing diamond surface and in the substrate-diamond interface are needed. An obvious candidate is the surface sensitive photoelectron spectroscopy, such as x-ray (XPS) and ultraviolet (UPS) photoelectron spectroscopy. EELS spectra can be obtained by x-ray excitaton of the C1s level. These XPS and EELS data show characteristic features for diamond, graphite, and carbides and therefore are valuable tools in order to discriminate between the grown species [1].

Experimental The diamond films were grown by a standard microwave plasma assisted chemical vapor deposition on a silicon substrate in a dilute mixture of methane in hydrogen. The concentration ratio of CH_4 to H_2 was 0.7% and the total pressure in the reaction chamber was maintained at 15 and 30 torr (in case 2 and case 1 respectively). The Si(100) wafer used as a substrate was polished with 3 μm diamond paste and ultrasonically cleaned in acetone prior to deposition. The temperature of the substrate, as monitored by an one-color pyrometer (case 1) and a alumel-chromel thermocouple (case 2), was 550°C and 950°C (for cases 2 and 1 respectively). In case 2 the deposition times for the samples were 0.5,1,2, and 4 hours (deposition took place at the edge of the plasma), while in case 1 they were 0.25,0.5,1,1.5,and 4 hours (and the samples were in the plasma). The system was continously pumped during deposition by a mechanical pump (total flux was 200 sccm).

The XPS (EELS) measurements were performed on a Leybold-Heraeus EA10/100 spectrometer using Mg K_α radiation with 1253.6 eV photon energy [2].

Results The results show that before exposure to the growth environment, the silicon surface was covered with a layer of SiO_2 and carbonaceous residue. Further, it was found by XPS (Fig. 2) that SiC formed after 0.25 h growth at the expense of some of the native oxides observed on the Si surface prior to deposition, while the carbonaceous residues were etched away. After 0.5 h growth, diamond was detected; but wether diamond nucleated on Si or SiC was not clear. We suppose that diamond nucleated on the SiC intermediate layer as well on eventual residuals of the diamond scratching emulsion. After 4 hours of growth, the SiC phase became undetectable in both cases (1 and 2), as diamond covered the whole substrate (Fig. 1,2).

Although there are some uncertanties in the measurement of the deposition temperature (different methods), one clearly observes a faster nucleation in the higher pressure, higher temperature case 1. We think this is due to the higher concentration of activated growth species in the ball-shaped plasma, such as CH_3 radicals, and to the higher amount of atomic hydrogen.

The EELS measurements confirm these results, showing only a SiC plasmon in case 2 (Fig. 2).

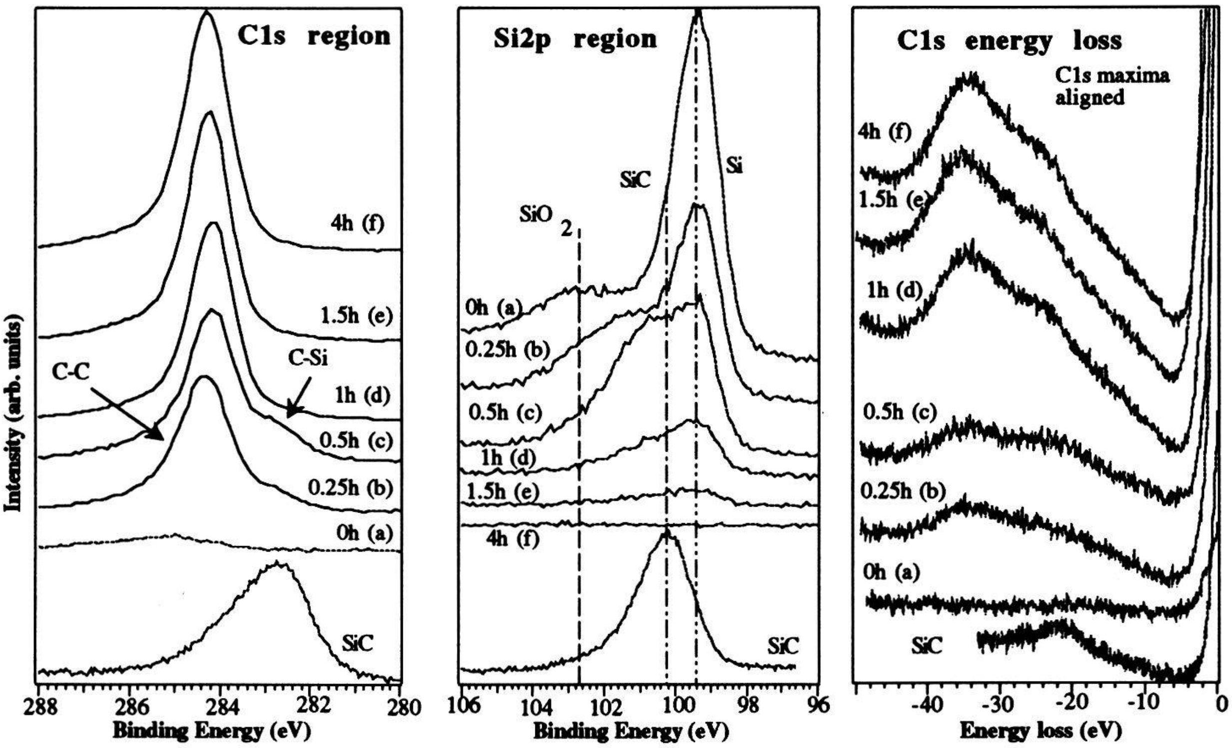

Fig.1 XPS spectra in the C1s-, Si2p-, and the C1s energy loss region of diamond films deposited at: T = 950°C , P = 30 torr, $CH_4 : H_2 = 0.7\%$

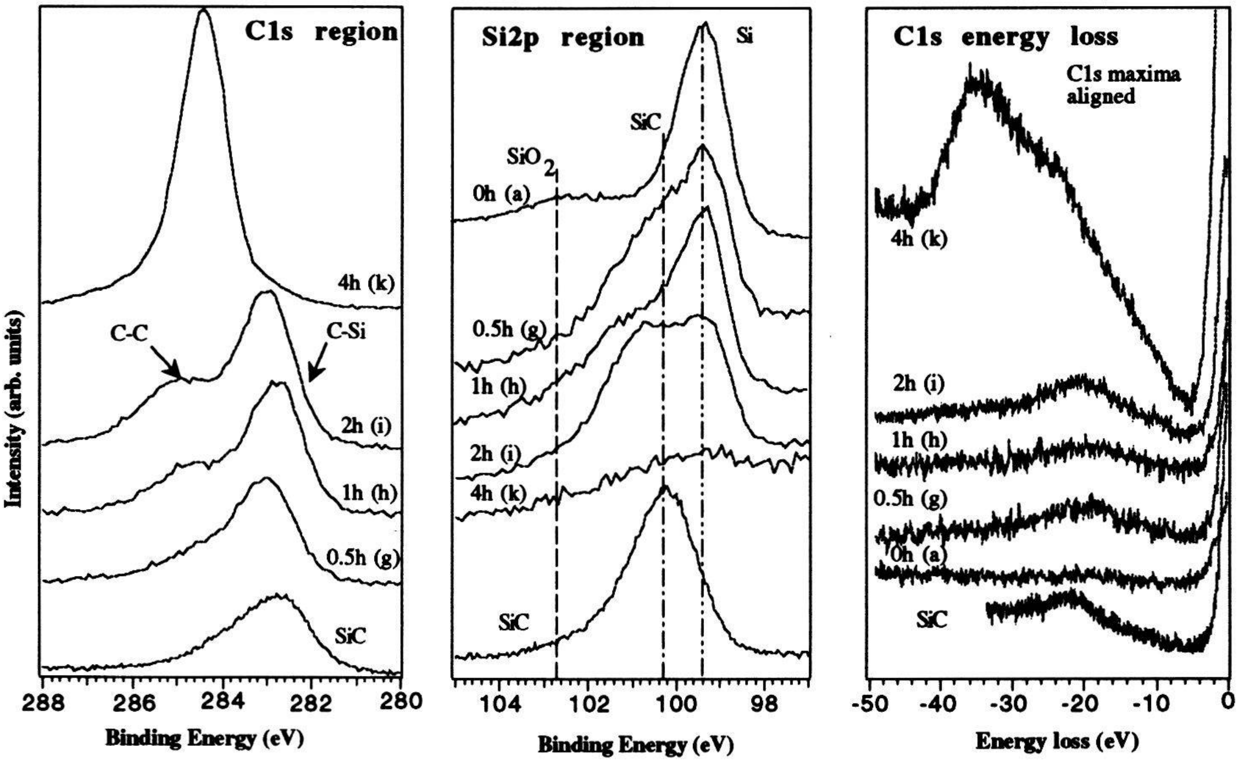

Fig. 2 XPS spectra in the C1s-, Si2p-, and the C1s energy loss region of diamond films deposited at: T = 550°C , P = 15 torr, $CH_4 : H_2 = 0.7\%$

Acknowledgement: Financial support of the Swiss National Science Foundation is greatfully acknowledged.

References: [1] David N. Belton, Steven J. Schmieg,J. Vac. Sci. Techol., **A8** (3) May/Jun 1990,2353-2362
[2] A. Mansour, G. Indlekofer, P. Oelhafen, Applied Surface Science, **48/49** (1991),312-318

Structure and growth of $YBa_2Cu_3O_{7-\delta}$ thin films on $Mg_2TiO_4(001)$

Part I. Growth conditions and film structure

L. Berthold, D. Hesse, R. Sum*, H.P. Lang*,
H. Haefke* and H.-J. Güntherodt*

Max Planck Institute of Microstructure Physics, Weinberg 2, D-O-4050 Halle, Germany
*Institute of Physics, University of Basel, Klingelbergstr. 82, CH-4056 Basel, Switzerland

Single-crystal Mg_2TiO_4 spinel layers have been used as a novel substrate for superconducting epitaxial $YBa_2Cu_3O_{7-\delta}$(YBCO) thin films. They have been grown on MgO(001) cleavage faces by a topotaxial solid-state reaction, and epitaxial YBCO thin films have been grown thereon. The structure and morphology of both Mg_2TiO_4 layers and $YBa_2Cu_3O_{7-\delta}$ thin films have been characterized by transmission electron microscopy and electron diffraction.

The search for suitable substrate materials is a significant part of the efforts to grow high-quality thin films of the high-T_c superconductors [1]. Among the criteria to be considered are the symmetry of the substrate lattice and its lattice parameters, the thermal expansion coefficient, and in particular the thermal and chemical stability of the substrate. Single-crystal MgO is one of the preferred substrates, but it is known to be rather reactive, in particular with the ambient air. We have found a method to considerably reduce this reactivity while preserving the advantageous properties of MgO as a substrate for epitaxial thin films of $YBa_2Cu_3O_{7-\delta}$ (YBCO) [2].

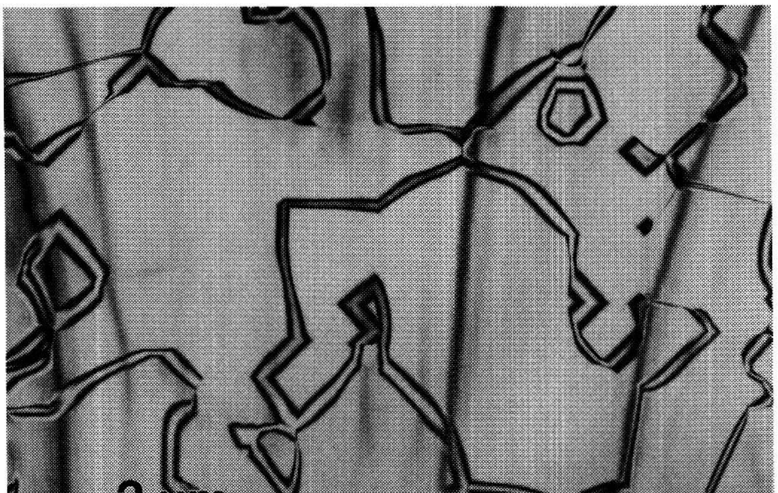

Figure 1: SAED pattern and TEM (220) bright-field image of a Mg_2TiO_4 film of 250 nm thickness.

Freshly cleaved (001) surfaces of MgO single crystals were mounted into a high-vacuum system, preheated there at 1250 °C for 20 min, and subsequently subjected to a TiO_2 vapour beam at a substrate temperature of 1100 °C. The vapour beam was generated by electron beam evaporation of an anatase powder target at a deposition rate of 0.05 nm/s. Under these conditions, perfectly oriented stoichiometric single-crystal Mg_2TiO_4 layers of 100 to 250 nm thickness were obtained, cf.[3]. Fig.1 shows an electron diffraction pattern and a TEM bright-field image of such a film. The orientation deduced from numerous diffraction patterns taken under various directions of beam incidence is

$$(001)\ Mg_2TiO_4 \parallel (001)\ MgO \quad ; \quad [100]\ Mg_2TiO_4 \parallel [100]\ MgO.$$

No lattice defects have been found in these films, with the exception of antiphase boundaries of the cation sublattice visualized in Fig.1 by a characteristic fringe contrast. RBS channeling (He^{4+}, 1.4 MeV) displayed a minimum yield value of $\chi_{min} \approx 5\%$.

Mg$_2$TiO$_4$ is an inverse spinel having a lattice parameter of 0.844 nm which is almost exactly twice that of MgO (0.4213 nm). Many of its properties are very similar to those of MgO, as e.g. the thermal expansion coefficient and the dielectric and optical properties. Mg$_2$TiO$_4$ is, however, characterized by a considerably lower reactivity with the ambient air than MgO [2]. Accordingly, it should represent a suitable substrate for YBCO thin films.

YBCO thin films were deposited by pulsed laser deposition in 27 Pa oxygen with a KrF excimer laser focussed to an energy density of 2.5 J/cm^2 onto a stoichiometric YBCO target. After preheating the substrates at 800 °C for 10 min, films of 150 to 200 nm thickness were obtained at different substrate temperatures between 600 and 800 °C. After deposition the films were cooled to 600 °C at a cooling rate of 4 K/min, followed by oxygen annealing at 10^{5}Pa and 500 °C for 30 min, and cooling down to room temperature.

Films deposited at substrate temperatures between 650 and 700 °C occurred to be homogeneously oriented according to the relationship

$$(001)\ \mathrm{YBCO}\ \|\ (001)\ \mathrm{Mg_2TiO_4}\ ;\ [100]\ \mathrm{YBCO}\ \|\ [100]\ \mathrm{Mg_2TiO_4}.$$

They have a low droplet density, display a regular surface structure characterized by growth hills, and are superconductive with T_c(onset) at 88 K (see Part II, this volume).

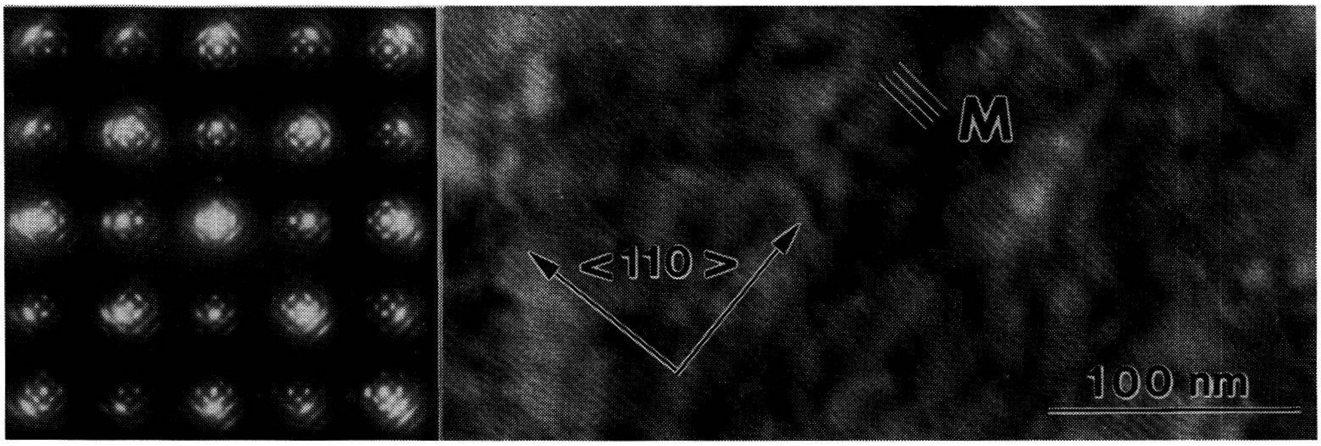

Figure 2: SAED pattern and TEM image of an YBCO film grown at 675 °C.

Fig. 2 shows an electron diffraction pattern and a TEM bright-field image of such a film. The good in-plane orientation of the YBCO film can clearly be recognized both from the diffraction pattern and the Moiré fringes in the image. Extensive double diffraction occurs in the diffraction pattern. Long linear defects along $\langle 110 \rangle$ directions have been found in the images. They have been attributed to twins. In YBCO(100) dark-field images characteristic contrast variations, frequently in form of dark regions of circular or elliptic shape have been found. They have been attributed to the spiral growth hills observed by STM (cf. Part II).

In summary, we have grown single-crystal Mg$_2$TiO$_4$ layers on MgO(001) substrates and have used them as a novel substrate for epitaxial YBCO thin films grown by pulsed laser deposition. As TEM and SAED have shown, at substrate temperatures between 650 and 700 °C the latter grow in uniform (001) orientation with good in-plane alignment.

REFERENCES

[1] T.Konaka, M.Sato, H.Asano, and S.Kubo, J.Supercond. 4, 283 (1991).

[2] D.Hesse, L.Berthold, H.P.Lang, H.Haefke, R.Sum, and H.-J.Güntherodt, Physica C (1992), in print.

[3] D.Hesse, J.Vac.Sci.Technol. A **5**, 1696 (1987).

Work supported by the German Federal Ministry of Science (BMFT 13N 5894) and by Swiss NSF.

Structure and growth of $YBa_2Cu_3O_{7-\delta}$ thin films on $Mg_2TiO_4(001)$

Part II. Orientation and growth morphology

R. Sum, H.P. Lang, H. Haefke, H.-J. Güntherodt,
L. Berthold* and D. Hesse*

Institute of Physics, University of Basel, Klingelbergstr. 82, CH-4056 Basel, Switzerland
*Max Planck Institute of Microstructure Physics, Weinberg 2, D-O-4050 Halle, Germany

Thin films of $YBa_2Cu_3O_{7-\delta}$ (YBCO) have been prepared by pulsed laser deposition on Mg_2TiO_4 substrate layers. Growth and morphology have been studied by scanning probe methods and X-ray diffraction. Different film morphologies could be related to YBCO(001), (100) and (103) orientations.

Various crystal materials which are commonly used as substrates for thin film preparation of high T_c superconductors (HTSC) [1] show surface degradation when stored in air. Especially MgO crystals react with water vapour and carbon dioxide forming hydroxide and carbonate, respectively, at the crystal surfaces. This can be avoided by a protective coating. It was found that Mg_2TiO_4 grown on MgO cleavage faces by a solid-state reaction [2] is a suitable protection layer. Comparing the lattice constants and thermal expansion coefficients of Mg_2TiO_4 and $YBa_2Cu_3O_{7-\delta}$ (YBCO), which are very similar, Mg_2TiO_4 might be an interesting new substrate for thin film growth of YBCO.

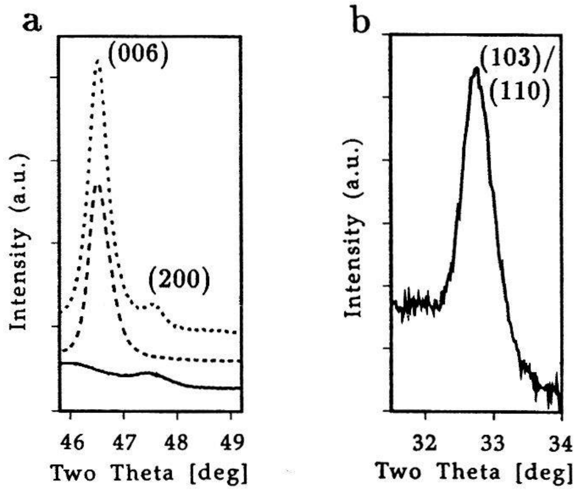

Figure 1: (a) XRD data for YBCO(006) and YBCO(200) reflections. (001) and (100) orientation for Y-725 (dotted line). Pure (001) orientation of sample Y-675 (dashed line). (100) orientation of Y-600 (solid line). (b) YBCO(103) or YBCO(110) reflection of sample Y-600.

Mg_2TiO_4 layers prepared in a single run have been used as substrate for YBCO thin film preparation (nominal film thickness 150 nm) by pulsed laser deposition [3] at different substrate temperatures T_s between 600 and 800 °C. Orientation and growth morphology of these samples were studied by X-ray diffraction (XRD) in Bragg-Brentano geometry (Θ-2Θ) and scanning tunneling microscopy (STM). STM has been carried out in air at room temperature. Using mechanically prepared $Pt_{90}Ir_{10}$ tips, images were taken in constant current mode applying a tip bias voltage of 800 mV and a tunneling current of 300 pA. Using several different tips for every sample tip-geometry induced artifacts should be widely excluded. (A sample prepared at $T_s = xxx$°C will be termed in the following Y-*xxx*.)

Fig. 1a shows the Cu K_α XRD data for YBCO(006) and YBCO(200) reflections of the samples Y-600 (solid line), Y-675 (dashed line) and Y-725 (dotted line). Sample Y-675 exhibits good (001) orientation whereas Y-725 shows additional (100) orientation demonstrated by the YBCO(200) peak. As seen in fig. 1b sample Y-600 is (103) or (110) oriented.

Fig. 2 shows three STM images of YBCO thin films grown at different substrate temperatures, *viz.* 600, 675 and 725 °C, respectively. Fig. 2a shows the surface of sample Y-600 indicating typical growth structures for (100) and (103) orientations. Slab-like grains are attributed to (100) oriented grains, whereas platelet structures (encircled) are assigned to (103) growth. Sample Y-675 exhibits a surface dominated by spiral growth hills (fig. 2b) originating from screw dislocations. The step height was determined to be of one unit - cell spacing in [001] direction. The average height variation of the growth hills is about 15 nm as obtained from STM line sections. Sample Y-725 shows a higher roughness than Y-675 and is additionally covered by (100) oriented grains (encircled grain in fig. 2c).

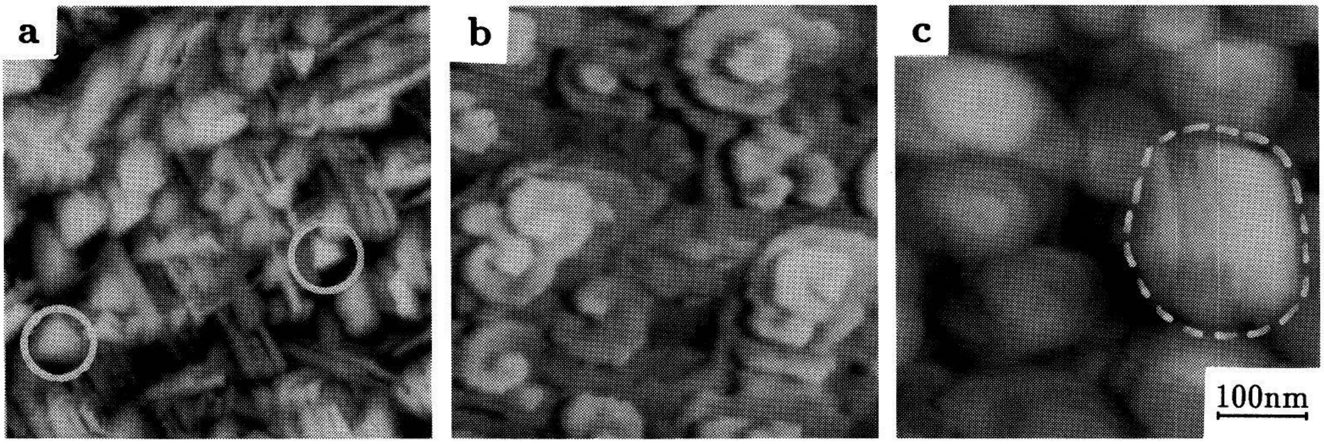

Figure 2: (a) STM image of sample Y-600 showing needles (attributed to (100) grains) and platelets ((103) grains). (b) Sample Y-675 with spiral growth hills. (c) Spiral growth hills and (100) oriented grain (encircled area) of Y-725.

Transition temperatures to superconductivity of the YBCO thin films have been measured by a *dc* four-probe method. Films grown at 675 °C show a transition with T_c (onset) at 88 K and a 90%–10% transition width of about 4 K.

In summary we have studied the growth of YBCO on novel Mg_2TiO_4 spinel layers grown on MgO cleavage faces. XRD and STM has been performed on a series of samples prepared at different substrate temperatures between 600 and 800 °C. At 675 °C YBCO thin films have been grown in (001) orientation. Below 675 °C mixed (100) and (103) growth appears whereas thin films grown above 675 °C exhibit (001) and additional (100) orientation. (001) oriented films show superconductivity with T_c (onset) at 88 K.

REFERENCES

[1] J.G. Bednorz and K.A. Müller, Z. Phys. B 64, 189 (1986).

[2] D. Hesse and H. Bethge, J. Cryst. Growth, **52**, 875 (1981), D. Hesse and H. Bethge, *ibid.* **65**, 69 (1983).

[3] D. Dijkamp, T. Venkatesan, X.D. Wu, S.A. Shaheen, N. Jisrawi, Y.H. Min-Lee, W.L. McLean, and M. Croft, Appl. Phys. Lett. **51**, 619 (1987).

Surface structure of cleaved $Bi_2Sr_{2.2}M_{0.8}Cu_2O_{8+\delta}$ single crystals (M = Ca, La) imaged by STM

H.P. Lang and H.-J. Güntherodt

Institute of Physics, University of Basel, Klingelbergstr. 82, CH-4056 Basel, Switzerland

Scanning tunneling microscopy images of cleaved $Bi_2Sr_{2.2}M_{0.8}Cu_2O_{8+\delta}$ single crystals (M = Ca, La) show a one-dimensional superstructure (period 27 Å) for the Ca-containing compound, whereas the La-containing compound is modulation-free. For both compounds, an atomic lattice (spacing 3.8 Å) is observed.

Evidence of superconductivity above 77 K in a Bi-Sr-Ca-Cu-O compound was first reported by Maeda *et al.* in 1988 [1]. A superconducting phase ($T_c = 80$ K) with an approximate stoichiometry of $Bi_2Sr_2CaCu_2O_8$ (in short BSCCO 2212) was rapidly identified [2,3]. The compound with an orthorhombic crystal structure ($a = 5.41$ Å, $b = 5.42$ Å, $c = 30.9$ Å, see tetragonal subcell with lattice constants $a_t = 3.8$ Å and $c_t = 30.9$ Å in fig. 1 for comparison) shows a one-dimensional (1d) superstructure modulation with a period of 27 Å in transmission electron microscopy [3,4]. The origin of this modulation was found to be due to insertion of an additional row of oxygen atoms between two rows of Bi atoms all ten rows of Bi atoms [5]. This leads to a deformation of the perovskite slab and therewith to a superstructure. Scanning tunneling microscopy (STM) imaging of this superstructure with atomic resolution on cleaved BSCCO 2212(001) single crystals has been obtained in ultrahigh vacuum or noble gas environment [6]. Substitution of certain elements in BSCCO 2212 leads to suppression of this modulation without affecting superconductivity (see Ref. 7 and Refs. cited therein). In this paper, we report on growth of BSCCO 2212 single crystals and the STM observation of the superstructure with atomic resolution. In crystals with the composition $Bi_2Sr_{2.2}La_{0.8}Cu_2O_{8+\delta}$ (BSLCO) [8] no modulation has been found by STM.

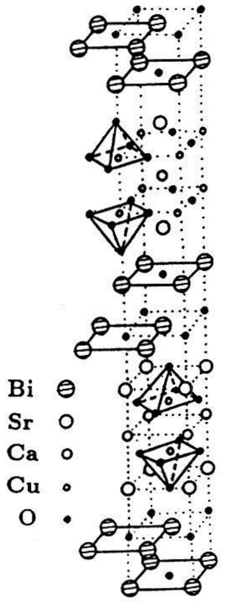

Fig. 1: Unit cell of BSCCO 2212.

Single crystals of BSCCO 2212 were grown by use of a self-flux technique. Appropriate amounts of analytical-grade powders of Bi_2O_3, $CaCO_3$, $SrCO_3$ and CuO were placed in an alumina crucible and melted in an electrically heated chamber furnace at about 970 °C for 24 h and then cooled to 820 °C at a typical rate of 2 K/h. Thereafter, the solidified melt was furnace-cooled to room temperature. Shiny BSCCO(001) crystal platelets were mechanically removed from the solidified matrix. The orientation of the platelets was confirmed by X-ray diffraction. The single crystals exhibit superconductivity at 80 K. BSLCO single crystals were

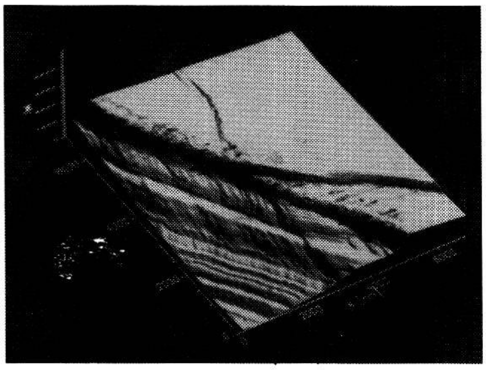

Fig. 2: Perspective STM view of the step structure of single-crystalline BSCCO 2212.

obtained by melting the appropriate mixture of the powders (using La_2O_3 instead of $CaCO_3$) at 1000 °C and cooling at a rate of 8 K/h to 800 °C, followed by furnace cooling.

STM was performed in a stainless steel glove box containing high purity argon. A gas purification system lowers the O_2, N_2 and H_2O impurity levels beyond our detection limit of 1 ppm. Prior to STM imaging, the crystals were cleaved in the glove box along the (001) direction to prepare an uncontaminated surface.

Fig. 2 shows the step and terrace structure of a BSCCO 2212 single crystal as observed by STM applying a tip bias voltage $U_t = 1$ V and a tunneling current $I_t = 1$ nA. In higher magnification, the STM reveals the 1d modulation having a period of 27 Å (fig. 3a). This superstructure is shown with atomic resolution in fig. 3b ($I_t = 0.6$ nA, $U_t = 140$ mV). The approximately square atomic lattice with an spacing of 3.8 Å is attributed to the Bi or O atoms in the Bi-O planes which represent the cleavage planes of BSCCO 2212. In figs. 3c and 3d, STM images of the atomic lattices of BSCCO 2212 and the isomorphic compound BSLCO are compared on the same scale. Both compounds show a square atomic lattice with a constant of 3.8 Å. In contrast to BSCCO 2212, BSLCO 2212 exhibits no long period modulation (fig. 3d).

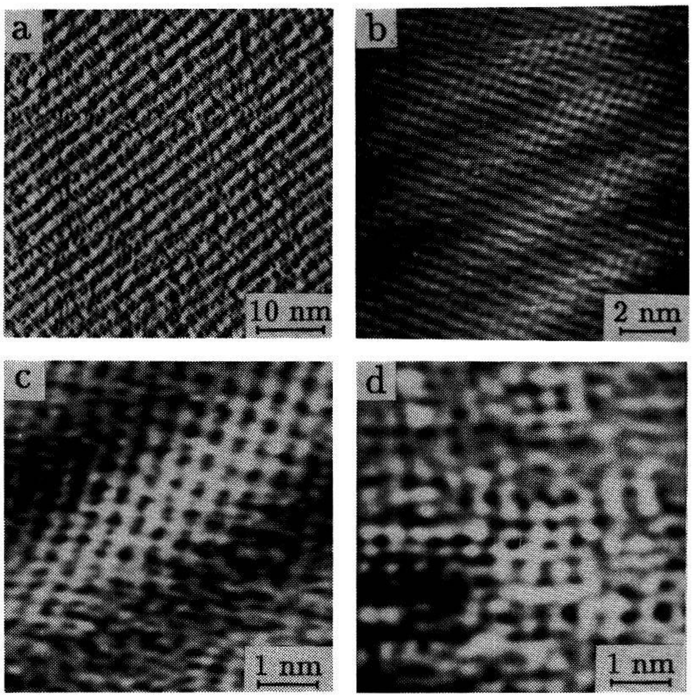

Fig. 3: (a) STM topview revealing the 1d modulation with a period of 27Å. (b) Atomically resolved modulation structure of BSCCO 2212. (c) Atomic resolution of the Bi-O plane in BSCCO 2212. Lattice constant 3.8 Å. (d) Atomic lattice (spacing 3.8 Å) of the BSLCO cleavage face.

REFERENCES

[1] H. Maeda, Y. Tanaka, M. Fukutomi and T. Asano, Jpn. J. Appl. Phys. **27**, L209 (1988).

[2] E. Takayama-Muromachi, Y. Uchida, A. Ono, F. Izumi, M. Onoda, Y. Matsui, K. Kosuda, S. Takekawa and K. Kato, Jpn. J. Appl. Phys. **27**, L365 (1988).

[3] R.M. Hazen, C.T. Prewitt, R.J. Angel, N.L. Ross, L.W. Finger, C.G. Hadidiacos, D.R. Veblen, P.J. Heaney, P.H. Hor, R.L. Meng, Y.Y. Sun, Y.Q. Wang, Y.Y. Xue, Z.J. Huang, L. Gao, J. Bechtold and C.W. Chu, Phys. Rev. Lett. **60**, 1174 (1988).

[4] Y. Matsui, H. Maeda, Y. Tanaka and S. Horiuchi, Jpn. J. Appl. Phys. **27**, L361, L372 (1988).

[5] Y. LePage, W.R. McKinnon, J.-M. Tarascon and P. Barboux, Phys. Rev. B **40**, 6810 (1989).

[6] M.D. Kirk, J. Nogami, A.A. Baski, D.B. Mitzi, A. Kapitulnik, T.H. Geballe and C.F. Quate, Science **242**, 954 (1988). C.K. Shih, R.M. Feenstra, J.R. Kirtley and G.V. Chandrashekhar, Phys. Rev. B **40**, 2682 (1989).

[7] J.M. Tarascon, W.R. McKinnon, Y. LePage, K. Remschnig, R. Ramesh, R. Jones, G. Pleizier and G.W. Hull, Physica C **172**, 13 (1990).

[8] S. Takebayashi, A. Maeda and K. Uchinokura, Annu. Rep. Eng. Res. Inst. Fac. Eng. Univ. Tokyo, **49**, 105 (1990).

MAGNETIC SHIELDING AND FLUX PENETRATION IN $(Y_1Ba_2Cu_3O_{7-\delta})_{1-x}Ag_x$ SINTERED TUBES

H. Castro[1] , E. Holguin[1] , J. F. Loude[2], H. Berger[3] and L. Rinderer[1]
[1] Institut de Physique Expérimentale, Université De Lausanne, 1015 Lausanne
[2] Institut de Physique Nucléaire, Université De Lausanne, 1015 Lausanne
[3] Institut de Physique Apliquée, Ecole Polytechnique Fédérale,1015 Lausanne

Abstract. We studied the effect of adding Ag on the shielding properties of YBaCuO tubular samples. The critical transport current J_{ct}, and trapped field Bi in the presence of an applied field H were measured. When H is suddenly switched on, we determined the times characterizing the dynamics of flux penetration. These times are compared with a theoretical model based on flux-flow regime.

Introduction

A polycrystalline high-T_c superconductor is formed by small grains (Abrikosov medium), typically of some microns, coupled by Josephson weak links. The critical transport current J_{ct} that flows through the sample depends on the properties of the Josephson medium and hence on the nature of the weak links (e.g. tunnel junctions, proximity bridges, twinned domains, etc). Therefore the addition of silver may alter some of these properties . Some authors have found that the $(YBaCuO)_{1-x}Ag_x$ ceramics resist better through ageing; others , an enhancement of the transport critical current. Here we present results of different kind of experiments performed on these ceramics with tubular geometry at 77K and for $x \leq 0.5$. We first study the strong dependence of J_{ct} on the applied field H under stationary conditions. Then, when H is suddenly switched on, we show typical Bi-H curves, where Bi is the trapped field in the hole. Finally, the penetration time t_o characterizing the dynamics of flux penetration was determined.

Results and discussion

The critical current density of the samples decreases exponentially (i.e. $J_{ct}(H) = J_1 + J_o\exp\{-H/H_o\}$) when a static field H is applied parallel to the cylinder axis, as shown in fig. 1. This behavior is also observed in the case x = 0, and can be attributed to the presence of weak links.

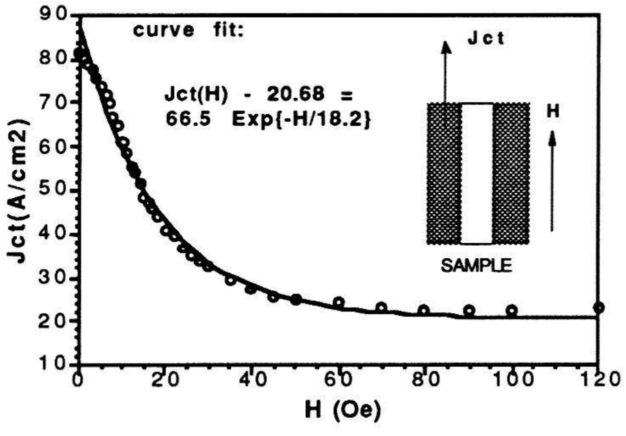

Fig. 1 Jc Vs. H for an YBaCuO sample with 30% Ag at T = 77K.

If at time t = 0 we abruptly switch on the external magnetic field from H= 0 to H > H*, where H* is the penetration field, the field penetrates through the outer surface of the sample and reaches the inner one after a time delay t_0. From this instant, a pickup coil placed in the hole begins to sense the magnetic flux. Fig. 2 shows typical Bi-H curves approaching the normal state curve asymptotically.

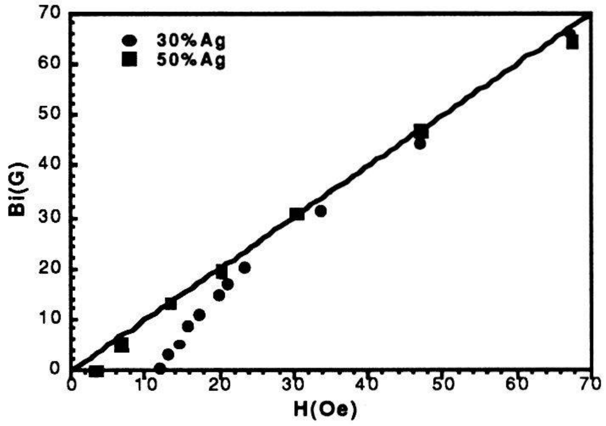

Fig. 2 Bi-H curves for samples containing 30% and 50% Ag .

In Figure 3 we have plotted the experimental results obtained for the delay time in the case x = 0.3. This is one of the times characterizing the phenomenon of flux penetration [1]. The theoretical curve was calculated according to the flux-flow theory presented by Ravikumar [2]. We observe some discrepancies on his theory for high values of the applied field. This can be due to extreme simplifications of the model, which neglects the complex structure of the ceramic.

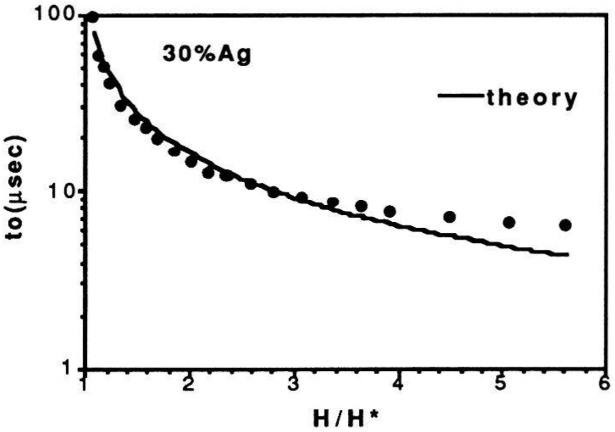

Fig. 3 Experimental and theoretical values of to Vs H/H* for x = 0.3.

Conclusions

Our experiments show that the addition of Ag to the YBaCuO material reduces the value of the penetration field H*, which is correlated to the critical current density in Bean's model [3]. Furthermore, the properties of these superconductors strongly depend on the Josephson medium. The theory developed by Ravikumar agrees quite well with our experimental results at low fields

References

[1] E. Holguin , J.F. Loude and H. Berger, Physica C 197 (1992) 167.
[2] G. Ravikumar, Solid State Commun. 77 (1991) 447.
[3] C. P. Bean, Phys. Rev. Lett. 8 (1962) 250.

Temperature Dependence of Anisotropic Resistivity in $Bi_2Sr_2CaCu_2O_{8+y}$ as a Function of Oxygen Content

Takashi YASUDA, Shuzo TAKANO* and Leo RINDERER

Institut de Physique Expérimentale, Université de Lausanne, 1015 Lausanne, Suisse
*Department of Computer Science and Electronics, KIT, Iizuka, Fukuoka 820, Japan

Temperature dependence of electrical resistivities ρ_{ab} (in plane) and ρ_c (out of plane) in $Bi_2Sr_2CaCu_2O_{8+y}$ has been measured with various oxygen annealing conditions ($10^{-5}<p<1$ bar and T=400°C). As a function of oxygen pressure p, dome-shaped curve of critical temperature was obtained. While $\rho_{ab}(T)$ exhibited a nearly linear T-dependence over the whole p range, nonmetallic $\rho_c(T)$ curve changed into metallic one with increasing p. Conduction mechanism is discussed by examining several possible functions for $\rho_c(T)$.

Doping property is one of the attracting features of the high T_c superconductivity (HTSC). Commonly in many HTSC cuprate oxides, carrier doping causes a drastic change from an antiferromagnetic insulator into a normal metal, and HTSC state appears at an intermediate region[1]. In $Bi_2Sr_2CaCu_2O_{8+y}$, many works on the hole density variation have been made on polycrystals by controlling oxygen content[2]. At present, however, basic properties involving anisotropy have not been clarified yet. In this work we present a series temperature dependence of anisotropic resistivity as a function of oxygen annealing pressure, that determines the excess oxygen content.

Thin plate-shaped single crystals were grown by KCl flux method[3,4]. Resistivities parallel and perpendicular to the CuO_2 plane were measured by Montgomery method with four probes, neglecting the anisotropy in CuO_2 plane. Oxygen content was controlled by annealing in various oxygen pressure ranged over $10^{-5} \leq p \leq 1$ bar with temperature fixed at 400°C. Homogeneity of oxygen content was examined from sharpness of the (0032)-peak by X-ray diffraction. In the range $10^{-4} \leq p \leq 1$ bar, samples with the size 0.5mm²x10μm became uniform after 15 hours of annealing. However homogeneity was not attained at $p<10^{-4}$ bar and resistivity data are shown only for $10^{-4} \leq p \leq 1$ bar below. We verified the variation of hole density by Hall measurement at room temperature with magnetic field up to 1.2 tesla.

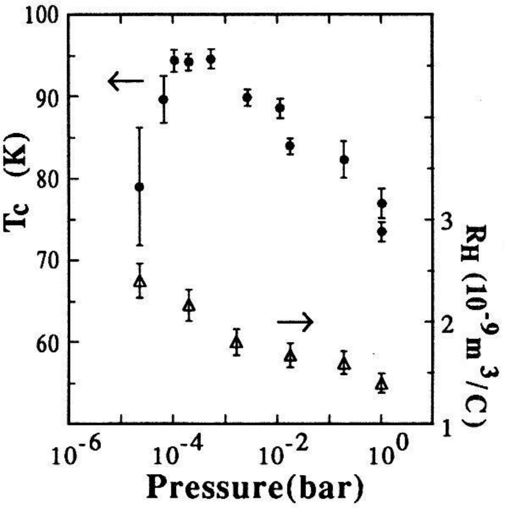

FIG. 1 Plot of T_c and R_H as a function of oxygen annealing pressure.

Figure 1 shows the oxygen pressure dependence of critical temperature T_c and Hall coefficient R_H. Transition width (10-90% recovery of normal ρ_c) is shown with bars for T_c. As the oxygen pressure increases, hole density (roughly $\sim 1/R_H e$) increases monotonously and a dome-shaped T_c curve is obtained consistently with the result on polycrystals[2].

Temperature dependence of in-plane resistivity ρ_{ab} is shown in Fig. 2. With increasing oxygen annealing pressure, normal resistivity decreases systematically, keeping an almost linear T-dependence. In the overdoped samples ($10^{-2} \leq p \leq 1$ bar), however, ρ_{ab}-T curves contain a certain amount of T^2-component, typically 5-10% of the linear term at 100K (p=1bar). It may be attributed to the electron-electron scattering in the context of Fermiology.

Figure 3 shows the temperature dependence of out-of-plane resistivity ρ_c. For $10^{-3} \leq p \leq 10^{-2}$ bar ($T_c \sim 85$K), the ρ_c-T curve is consistent with the result measured on as-grown samples[5]. The remarkable resistive upturn at $p = 10^{-4}$ bar becomes negligible at 1bar. Since the whole data were taken from the same sample with same electrodes, the metallic behavior is not due to the defect-induced contribution of ρ_{ab}. In order to identify the origin of the upturn, we attempted a curve fitting for the data at $p > 10^{-2}$ bar with some possible functions $f(T)$, using $\rho_c(T) = A + BT + f(T)$. As a result, we could reproduce data with several functions: $f_1(T) = C\exp(T_0/T)$ (with T_0 distributed over 400-700K owing to sample dependence), $f_2(T) = C/(T-T_0)$ (with $T_0 < T_c$) and $f_3(T) = CT^{-\alpha}$ (α=3-7). On the other hand, either the variable-range-hopping type function $\exp[(T_0/T)^{1/(d+1)}]$ or T^{-1} contribution predicted in the early report by Anderson and Zou (AZ)[6] was not applicable to the curves in Fig. 3. Since onset value of localization can be estimated at an order of 1mΩcm assuming a spheroidal Fermi surface and $n \sim 10^{21}$cm^{-3}, explanation of high ρ_c value in terms of a short mean free path leads to discrepancy with the metallic behavior. As an alternative conduction mechanism, we can possibly keep the first part of AZ theory, that the conduction is caused by single particle tunneling between insulating layers (BiO). In this scheme, one of the fit function $f_1(T)$ can be interpreted as a thermal hopping of holes between metallic layers through the energy gap of BiO layer. Our result $T_0 \sim$400-700K gives a fair agreement with the E_v value 0.05eV(~580K) measured by Scanning Tunnelling Microscopy[7]. The diminution of resistive upturn at p=1bar implies that some part of excess oxygen creates impurity band in the energy gap of BiO layer.

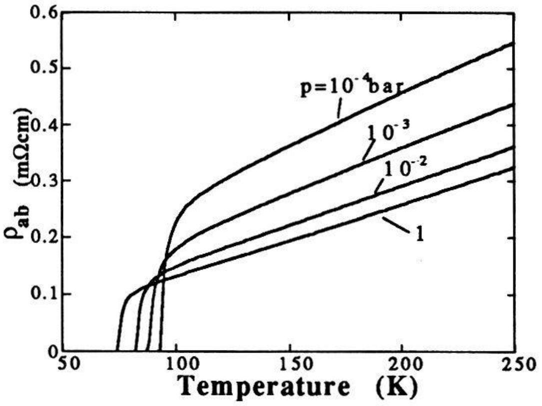

FIG. 2 Temperature dependence of ρ_{ab} as a function of oxygen annealing pressure.

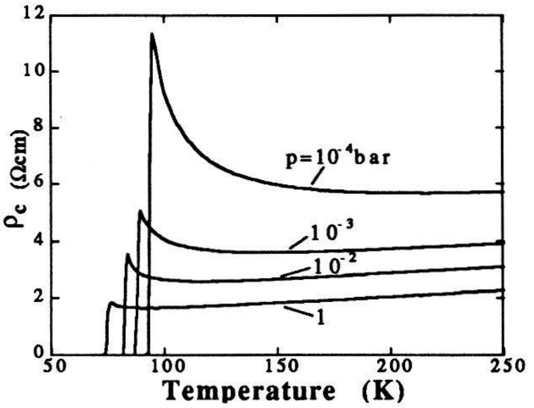

FIG. 3 Temperature dependence of ρ_c as a function of oxygen annealing pressure.

References

[1] J. B. Torrance, Y. Tokura, A. I. Nazzal, A. Bezinge, T. C. Huang and S. S. P. Parkin, Phys. Rev. Lett. **61**, 1127 (1988).
[2] G. Triscone, J.-Y. Genoud, T. Graf, A. Junod and J. Muller, Physica **C176**, 247 (1991).
[3] T. Yasuda and S. Takano, Jpn. J. Appl. Phys. **30**, L349 (1991).
[4] T. Yasuda and S. Takano, Jpn. J. Appl. Phys. **31**, 1340 (1992).
[5] K. Kadowaki, A. A. Menovsky and J. J. M. Franse, Physica **B165-166**, 1159 (1990).
[6] P. W. Anderson and Z. Zou, Phys. Rev. Lett. **60**, 132 (1988).
[7] T. Hasegawa and K. Kitazawa, Jpn. J. Appl. Phys. **29**, L434 (1990).

Inverse Method for the Crystal Field in MT_2X_2 Compounds ($M = Pr, U$; $T =$ transition metal; $X = Si, Ge$)

P. Santini and G. Amoretti*
Institut de Physique Théorique, Université de Lausanne, CH-1015 Lausanne, Switzerland†
A. Blaise
DRFMC/SPSMS, Centre d'Etudes Nucléaires de Grenoble, 85X, F-38041 Grenoble, France
R. Caciuffo
Dipartimento di Scienze dei Materiali, Università di Ancona, I-60131 Ancona, Italy

We have developed a method, based on a suitable inversion of the crystal-field eigenproblem, which allows us to estimate the value of the crystal-field parameters for magnetically ordered $J = 4$ tetragonal compounds. We applied the method to UPt_2Si_2, $PrFe_2Si_2$ and $PrFe_2Ge_2$, and found their properties to be well described by the crystal-field model.

The f_2 and f_4 configurations have a $J = 4$ multiplet as ground manifold. The properties of several interesting U and Pr systems presenting localized electron behavior are thus conveniently described in terms of the crystal electric field (CF) acting on this multiplet. In particular, compounds having $ThCr_2Si_2$- or $CaBe_2Ge_2$-type structure are characterized by a tetragonal CF at the magnetic site. This family of compounds is quite interesting since it contains some well-known Kondo lattice and heavy fermion systems, in which effects associated with Kondo-like screening or partial delocalization of the f electrons can introduce important corrections of the predictions of CF theory. Our purpose is to develop a method permitting us to analyse easily the full range of possible solutions of the CF model which can account for the observed phenomenology, if such solutions exist. We concentrate on the case in which the CF ground state is a singlet, and the ordered magnetic moment lies along the c-axis, as is common in this family of compounds. The case of a singlet ground state is particularly interesting, since a Van Vleck-type induced magnetic order can exist and a wide variety of behaviors can occur, depending on details of the CF splittings.

By properly inverting some of the equations appearing in the CF secular problem, we are able to impose *a priori* some experimental constraints: in particular, the values of the ordered moment at $T = 0$ and of the ordering temperature are imposed in a self-consistent way within a molecular field approach. Other conditions we impose are the splitting with one excited singlet, which can be measured in a neutron scattering experiment, and one coefficient characterizing the ground state composition, which affects neutron scattering intensities.

The method was applied to UPt_2Si_2, which orders antiferromagnetically at $T_N = 35$ K with $\mu_{\text{ord}} = 1.67\,\mu_B$, and was shown by inelastic neutron scattering to present well-defined peaks, which were attributed to CF transitions [1]. A previous theoretical analysis [2] of the magnetic and thermodynamic properties of UPt_2Si_2 failed to explain in a unique model the neutron data and the ordered moment, which was calculated to be $\mu_{\mathrm{ord}} = 2.8\,\mu_B$. The difference was attributed to Kondo compensation. By our method we find that this assumption is not necessary, since this system can be described satisfactorily in the frame of the CF model. The experimental data, and in particular the position and intensity of the neutron peaks, are enough to select a very small class of acceptable CF parameters.

We also considered two compounds of Pr^{3+}, namely $PrFe_2Si_2$ and $PrFe_2Ge_2$, ordering at $T_N = 7.7$ K and $T_N = 14.2$ K, respectively. After imposing the values of the ordered moment and the ordering temperature, and using the value of B_{20} derived from Mössbauer data on the homologous *Gd* compound, we are left with 3 free CF parameters. There is only a small range of variation for these 3 parameters in which solutions exist. The two very different values of the ordered moment at $T = 0$ ($1.4\,\mu_B$ and $2.75\,\mu_B$) and of the ordering temperature, can be reproduced in the frame of the same CF model. This is in agreement with the results of an *ab initio* model developed in [3]. We find that slight modifications in the low-lying group of CF levels are responsible for the different characteristics of the magnetic ground states of these compounds. These small quantitative differences can yield two very dissimilar behaviors because the moment is induced by the magnetic coupling of the ground state with the excited states. Small modifications of these latter may thus have strong effects on the magnetic properties.

For these *Pr* compounds, neutron inelastic scattering experiments are in progress, which will enable us to verify and refine the model.

* Permanent Address: Dipartimento di Fisica, Università di Parma, I-43100 Parma, Italy.

† Work supported in part by the Swiss National Science Foundation, Grant N° 20-28846.90.

References

[1] R.A. Steeman, E. Frikkee, C. van Kijk, G.J. Niewenhuys, A.A. Menovsky, J. Magn. Mat. **76-77**, 435 (1988).

[2] G.J. Niewenhuys, phys. Rev. B**25**, 5260 (1987).

[3] M. Malaman, G. Venturini, A. Blaise, G. Amoretti and J.P. Sanchez, J. Magn. Mat. **104-107**, 1359 (1992).

BRILLOUIN SCATTERING ON UTe SINGLE CRYSTALS

M.Mendik and P.Wachter

Laboratorium für Festkörperphysik, Eidgenössische Technische
Hochschule Zürich, 8093 Zürich, Switzerland

Surface acoustic phonons on UTe single crystals coated with thin Pt films have been measured by means of Brillouin light scattering at room temperature and at 81°K (i.e. below T_C of ferromagnetic ordering). Some elastic properties of UTe have been derived from the angular dependent velocity of surface acoustic phonons and evidence for a negative C_{12} below T_C has been found.

Anomalies of the phonon dispersion curves of the rocksalt structure uranium compounds UX (X=Te,Se) have been first observed by neutron scattering [1]. Negative Poisson's ratios and soft bulk moduli, that are typical signs for intermediate valence behavior, have been estimated from the phonon dispersion curves but with rather large error bars. Extensive ultrasonic studies on UX compounds [2] confirmed a negative C_{12} for both USe and UTe at room temperature whereas low temperature measurements, were not possible due to strong attenuation below T_C (UTe and USe order ferromagnetically below Curie temperatures T_C=160° and 102°K.). This motivated us to perform low temperature Brillouin scattering measurements, that sample phonons in the GHz range, in order to look for a possible coexistence of magnetism and intermediate valence behavior.

For the measurements we used the TM polarized λ=514 nm line of an Ar laser as the excitation source. The power on the sample was held below 50 mW. The backscattered light was analyzed by a (3+3) pass Fabry–Pérot tandem interferometer [3]. During all experiments the sample was in He exchange gas mounted in a lN_2 optical cryostat. The measurements were performed at room temperature and 81°K.

The fabrication of UX single crystals is described in [4]. All UTe single crystals have been cleaved along (100) planes in a He glove box. In order to prevent surface damage caused by the incident laser beam thin Pt film have been deposited on the (100) oriented planes (by RF planar magnetron sputtering with Pt target purity: 99.999%). The film thicknesses have been finally checked by Rutherford backscattering (RBS).

In contrast to transparent materials UX are opaque (for λ=514nm). Hence only surface excitations are detected by BS. The velocity of phonons localized at the surface (surface acoustic waves, SAW) is a function of both the elastic properties, the density ρ and the direction of the wavevector $\mathbf{k}_p$ in the sample plane. Since the penetration depth of the SAW's detected by BS is in the order of 4000Å the SAW's carry information about the elastic properties of the whole bulk. Moreover, from the angular dependence of the velocity of SAW's on basal planes of cubic crystals it is possible to fit the complete elastic tensor [5,6]. The presence of thin Pt films (thickness h<170Å) caused a vanishingly small influence (<1%) to the velocity of the SAW propagating on the bare substrate.

Fig.1) shows the angular dependence of the velocity of SAW's on a UTe(100) single crystal covered with Pt (h=170Å). Triangles (▲) denote measurements at room temperature and dots (●) measurements at 81°K. The line has been calculated using the values obtained from ultrasonic measurements [2], i.e.C_{11}=143.4 GPa; C_{44}=11.9 GPa; C_{12}=–20.75 GPa. Within the error of 1–2% no changes of the SAW velocity as a function of the direction have been observed both for room temperature and at 81°K. This is the sign for elastic "quasi" isotropy (i.e. The anisotropy ratio $\eta=2\cdot C_{44}/(C_{11}-C_{12})$ is smaller than one which is in general found in most material crystallizing in the fcc rocksalt structure.). In addition, no remarkable changes of the SAW velocity have been

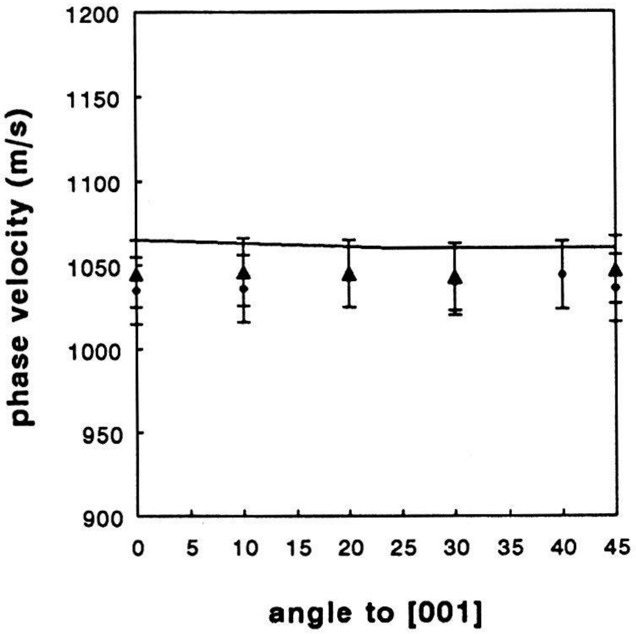

Fig.1)

observed below the T_c for magnetic ordering that is accompanied by a slight cubic to rhombohedral lattice distortion.

The velocity of SAW's on quasi isotropic materials is closely related to the lowest bulk pure shear wave velocity $v_{shear}^2=(C_{44}/\rho)$. Therefore, the velocity of SAW's can be expressed as $v_{saw} = \beta \cdot v_{shear}$ with $0.9<\beta<1.0$ [7]. Thus we obtain for $C_{44}=11.4$ GPa, which is in agreement with [2]. From the angular dependence of the SAW velocity we have fitted C_{11} and C_{12}, keeping the density $\rho=10.41$ gr/cm³ and $C_{44}=11.4$ GPa constant. The best fit has been obtained with: $C_{11}=(159\pm30)$ GPa and $C_{12}=(-20\pm50)$ GPa. In addition, combining the formulae for the anisotropy ratio $\eta<1$ and the bulk modulus $B={}^1/_3\cdot(C_{11} + 2\cdot C_{12})$ we obtain an upper boundary for C_{12}: $C_{12} < B - {}^2/_3\cdot C_{44}$. With B=34GPa [2] we calculate $C_{12} < 26$ GPa.

In conclusion, we have performed Brillouin scattering on UTe single crystals both at room temperature and at 81°K. The result from our fit as well as the measured velocities of the SAW's at 81°K indicate that the elastic properties of UTe do not change significantly below T_C.

The authors wish to acknowledge K.Mattenberger for crystal growth and characterization, A.Weber for fabricating the Pt films and C.Schwarz for RBS analysis.

[1] T.M.Holden, W.J.L.Buyers, E.C. Svensson, J.A.Jackman, A.F.Murray, O.Vogt and P.de V.DuPlessis, *Journal of Applied Physics* **53** 1967 (1982).
[2] J.Neuenschwander, O.Vogt, E.Voit and P.Wachter, *Physica* **144B**, 66 (1986).
[3] J.R.Sandercock, *Solid State Communications* **26**, 57 (1978).
[4] K.Mattenberger, L.Scherrer, O.Vogt, *Journal of Crystal Growth* **67**, 467 (1984).
[5] M.W.Elmiger,J.Henz,H.von Känel,M.Ospelt and P.Wachter, *Surface and Interface Analysis* **14**, 18 (1989).
[6] M.Mendik, S.Sathish, A.Kulik, G.Gremaud and P.Wachter, *Journal of Applied Physics* **71**, 2830 (1992).
[7] G.W.Farnell in "*Physical Acoustics*", Ed. W.P.Mason, Vol.6 (Academic Press, N.Y., 1970) pp.109–166.

Spin-Polarized Photoemission from $In_xGa_{1-x}As/GaAs$

J.C. Gröbli, A. Vaterlaus, D. Guarisco, H. Hepp, and F. Meier,
Laboratorium für Festkörperphysik, ETH Hönggerberg,
CH-8093 Zürich, Switzerland
Y. Yashin(1), Y. Mamaev(1), B. Yavich(2), and I. Kochnev(2)
(1) St.Petersburg Technical University, Division of Experimental Physics, St.Petersburg, Russia
(2) A.F.Ioffé Institute, Russian Academy of Sciences, St.Petersburg, Russia

By excitation with circularly polarized light up to 80 % spin - polarized photoelectrons are emitted from strained $In_xGa_{1-x}As$ (x=0.15) layers grown on GaAs.

Highly polarized electron sources based on photoemission are an important tool in many branches of physics [1,2]. The standard source today is GaAs: Electrons excited by circularly polarized light from the valence band maximum (VBM) to the conduction band minimum (CBM) have a spin-polarization of P=50 % [3]. By alternate deposition of cesium and oxygen onto the surface of a p-doped GaAs crystal the vacuum level can be lowered below the CBM (state of negative electron affinity: NEA) such that the polarized excited electrons are photoemitted. The 50 % - limit is imposed by the fact that in GaAs two antiparallel polarized excited states are populated simultaneously. This can be avoided by lifting the orbital band degeneracy at VBM [4,5]. Then only one transition occurs into a completely polarized final state.

In this work the removal of the degeneracy at the VBM is achieved by growing an epitaxial overlayer of $In_xGa_{1-x}As$ (x=0.15) onto a GaAs(001) substrate. The lattice mismatch between the overlayer and the substrate induces a tensile (not compressive !) strain and thereby a tetragonal distortion of the overlayer which lifts the band degeneracy at the VBM. The

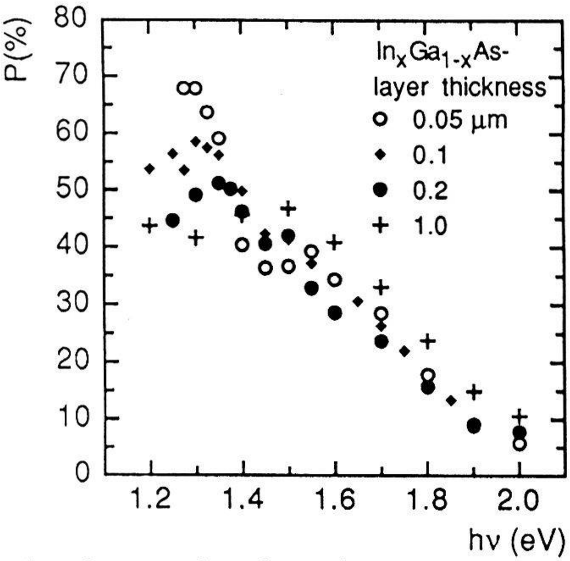

Fig.1. Polarization of the total yield of optically spinoriented photoelectrons. The sample temperature was 220 K.

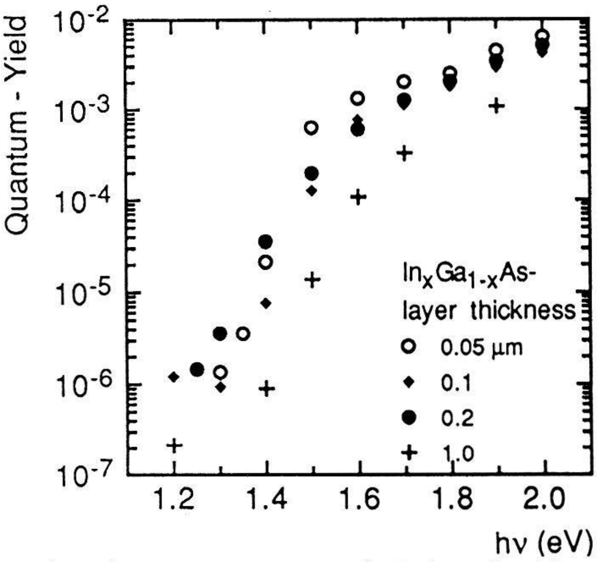

Fig.2. Quantum yield of the same samples as used for the P(hν) measurements.

epitaxial structures prepared at the Ioffé-Institute were uniformly p-doped with Mg: $p = 5x10^{18}$ cm^{-3}.

Fig.1 shows the polarization spectra P(hν) of the total photoyield for samples with an overlayer thickness of 0.05, 0.1, 0.2, and 1.0 μm. The temperature of the sample was 220 K. For the thinnest layer the polarization is largest. This is attributed to the fact that the strain in these layers is rather uniform. For thicker layers the strain relaxes which leads to a reduction of the polarization. The threshold polarization of the 1 μm overlayer is identical to the one of unstrained bulk GaAs.

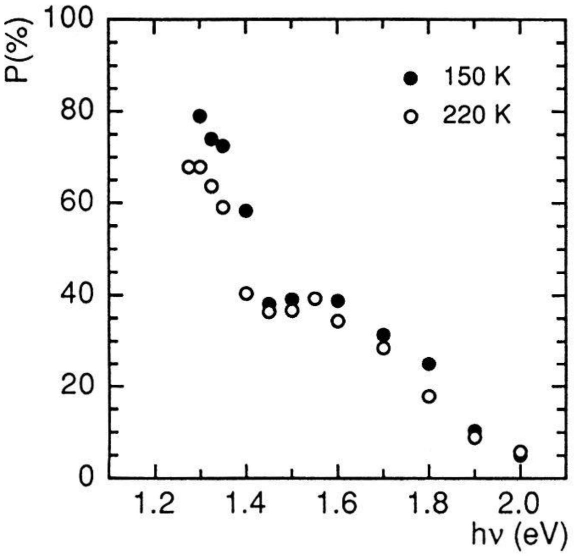

Fig.3. Polarization of the total yield of optically spinoriented photoelectrons emitted from the 0.05 μm thick $In_xGa_{1-x}As$.

Fig.2 shows the quantum yield - the number of emitted electrons per incident photon - for the same samples from which the polarization data were obtained. The quantum yield near photothreshold is untypical for NEA. It does not exhibit the characteristic step function-like increase at the photothreshold. We conclude that the samples described in this paper had a small positive electron affinity. The threshold polarization could be increased from 70 % up to 80 % by cooling the thinnest sample down to T = 150 K, see Fig.3.

We thank H.C. Siegmann for stimulating discussions and K. Brunner for the expert technical assistance. The financial support by the Schweizerische Nationalfonds is gratefully acknowledged.

References

[1] D.Pierce and J.Celotta in "Application of Polarized Electron Sources" (Editors: F. Meier and B. Zakharchenya), Modern Problems in Condensed Matter Sciences 8, 295 (1984)

[2] J. Kessler, Adv. in Atomic, Molecular, and Optical Phys.27, 81 (1991)
J. Kirschner, Polarized Electrons at Surfaces, Springer,Berlin (1985)

[3] F. Meier and D. Pescia in "Optical Orientation" (Editors: F. Meier and B. Zakharchenya), Modern Problems in Condensed Matter Sciences 8, 295 (1984)

[4] T. Maruyama, E. Garwin,R. Prepost, G. H. Zapalac, J. S. Smith, J. D. Walker, Phys. Rev. Lett. 66, 2376 (1991)

[5] T.Nakanishi, H.Aoyagi, H.Horinaka, Y.Kamiya, T.Kato,S.Nakamura, T.Saka, and M.Tsubata, Phys. Rev. Lett.A158, 345 (1991)

Correlations in the Quantum Ising Spin-Glass in a Transverse Field

Ferenc Pázmándi, Zbigniew Domański and Paul Erdős
Institute of Theoretical Physics,
University of Lausanne, CH-1015 Lausanne, Switzerland

The boundary between the paramagnetic and glass phases of the quantum Ising spin-glass in a transverse field is calculated using a new type of approximation. The agreement with numerical results is better than that obtained by previous theories.

The quantum Ising spin-glass in a transverse field is defined by the Hamiltonian

$$H = -\sum_{i \neq j}^{N} J_{ij}\sigma_{zi}\sigma_{zj} - K\sum_{i=1}^{N}\sigma_{xi}. \tag{1}$$

Here, $\sigma_{\alpha i}$ are the Pauli spin matrices referring to the i-th member of an ensemble of N spins ($\alpha = x, y, z$; $i = 1, \ldots, N$), and K is the strength of the transverse field. The spin interaction coefficients J_{ij} are a set of Gaussian random variables with zero mean and variance N^{-1}.

The model described by (1) undergoes a transition between the paramagnetic (P) and spin-glass (SG) phases as a function of the temperature T and transverse field strength K. No theory exists to calculate exactly the boundary between these two phases. Numerical methods based on the Trotter-Suzuki transformation give the phase boundary drawn as a solid line in Fig. 1 [2, 3].

The purpose of this work is to develop a reliable theoretical approximation for the paramagnetic free energy $F_p(T, K)$, from which the phase boundary can be calculated. We compare previous theoretical results [4, 5, 6, 7] and our own with the results of the numerical work [2, 3].

The free energy is expressed using the replica method and performing a quenched average over the random variables [3]. The difficulty caused by the non-commutativity of the spin operators is circumvented by the Trotter-Suzuki transformation [1]. This introduces an additional dimension to the problem, with new variables whose number P has to be made infinite in order to make the transformation accurate. The numerical results quoted above have been obtained for P of order 10, and subsequently extrapolated to $P \to \infty$.

In our approach, we express the thermal average spin-spin correlation function $\langle \mu^t \mu^{t'} \rangle$ of the Trotter variables μ^t as the sum of a constant q_0 and a correlation $C(t - t')$. The paramagnetic free energy is then evaluated considering the term $C(t - t')$ as a perturbation. For $q_0 = 0$ in the second order of the perturbation we obtain the phase boundary represented by the dashed line in Fig. 1. For $q_0 \neq 0$ in the first order of the perturbation one obtains the dash-dotted line in Fig. 1.

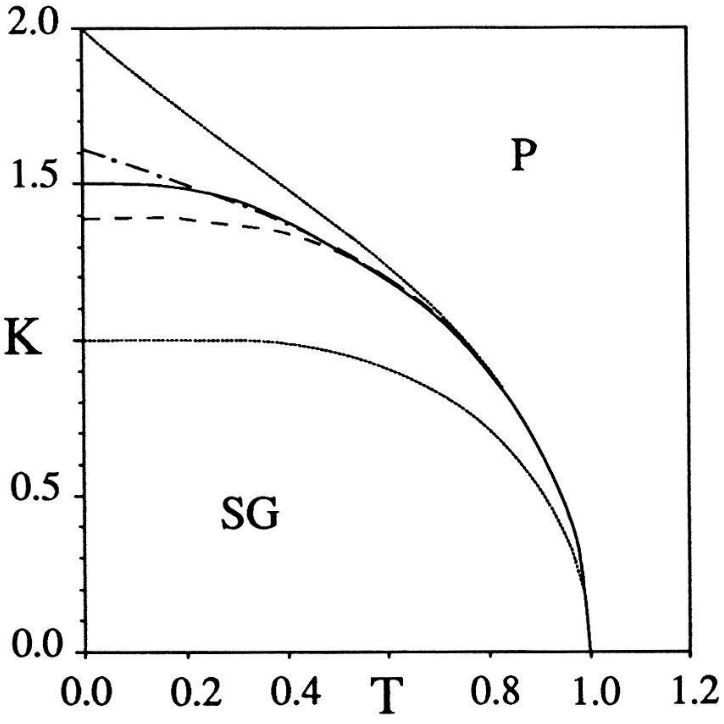

Fig. 1.

Phase transition lines for the Ising spin-glass in a transverse field.
P: paramagnetic phase;
SG: spin-glass phase.

It may be seen that this is a much better approximation to the "exact" numerical phase transition line, than previous results [4, 5, 6, 7]. In particular, for $T = 0$, previous theories either obtained $K_c = 1$, which is simply the static approximation with $q_0 = 0$, or $K_c = 2$ with $q_0 \neq 0$. Our results $K_c = 1.388$ for $q_0 = 0$ (respectively $K_c = 1.612$ for $q_0 \neq 0$) could even be further improved by taking into account higher-order spin-spin correlations.

The support of the Swiss National Science Foundation through grant 20-28846.90 is gratefully acknowledged.

References

[1] R.M. Stratt, Phys. Rev. B**33**, 1921 (1986);

[2] T. Yamamoto and H. Ishii, J. Phys. C : Solid State Phys. **20**, 6053 (1987).

[3] K. Usadel and B. Schmitz, Solid State Commun. **64**, 975 (1987).

[4] Q. Jiang and Z.Y. Li, Phys. Rev. B**40**, 11264 (1989).

[5] T.K. Kopeć, K.D. Usadel and G. Büttner, Phys. Lett. A **150**, 70 (1990).

[6] K.D. Usadel, G. Büttner and T.K. Kopeć, Phys. Rev. B**44**, 12583 (1991).

[7] L. De Cesare, K. Lukierska-Walasek and K. Walasek, Phys. Rev. B **45**, 8127 (1992).

Epitaxial $KTa_{1-x}Nb_xO_3$ layers for pyroelectric detectors

D. H. Jundt, R. Gutmann, and P. Günter

Institute of Quantum Electronics, ETH-Hönggerberg, CH–8093 Zürich

Ferroelectric epitaxial layers of $KTa_{1-x}Nb_xO_3$ have been grown form a KF–KTN solution on (100) $KTaO_3$ substrates. Lattice matching of the 5 to 30 μm thick films was achieved by adding a certain percentage of NaF to the melt. The incorporation of Na in the crystal decreases the lattice constant of the film which can be utilised to influence the domain behaviour. The stoichiometry x of the layers is chosen to yield ferroelectric films at room temperature. The temperature and frequency dependence of the pyroelectric voltage response of the poled layers have been measured.

Thin films of ferroelectric crystals are of interest for integrated optic and sensor applications. Optical modulators and optical frequency conversion devices benefit from the large nonlinerities and the low losses typically seen in ferroelectric oxide materials. Pyroelectric sensors have improved speed characteristics when the active layer thickness is reduced.

Monocrystalline $KTa_{1-x}Nb_xO_3$ (KTN) films of good quality can be grown on (100) $KTaO_3$ substrates [1]. While $KTaO_3$ belongs to a cubic crystal class, KTN undergoes a series of phase-transitions on cooling depending on the niobium content. The paraelectric-ferroelectric transition takes the structure from the cubic m3m to the tetragonal crystal class 4mm. For Nb compositions around x=0.45, the Curie temperature is around $T_C \approx 60°C$ resulting in large dielectric constants, nonlinear-optic, electro-optic, and pyro-electric coefficients in the tetragonal phase at room temperature [2]. The ferroelectric layers are grown by liquid phase epitaxy (LPE) from a KF solution containing 8 mol% KTN at a temperature around 900°C [3]. Because of a difference in distribution coefficient between Ta and Nb, the Nb content of the melt has to be x=0.82 in order to produce a film with x=0.45. The lattice constant (at T>70°C, cubic) of the resulting film is larger than that of the substrate which leads to films containing misfit dislocations. The addition of NaF to the melt results in a film where a part of the K-lattice sites are filled by Na^+ ions leading to a reduction of the film lattice constant. By varying the amount of added NaF, one can adjust the lattice constant of the film. In this way, lattice matched films of cubic symmetry have been grown successfully [3]. Lattice matching of ferroelectric films is more complicated because of the structural phase-transition near the Curie temperature. The dimensions of the crystal unit cell changes upon cooling through the phase transition. The c-axis (defined as the polar axis) can lie along any of the three cubic crystal axes of the high temperature phase. The cell expands along the c-axis, whereas it contracts slightly in the two perpendicular directions. Small Na contents favour a spontaneous polarisation direction perpendicular to the film plane whereas large Na contents favour a c-axis direction in the film plane. The samples investigated here were grown from a solution with a NaF:KF ratio of 0.2. The film, grown at 926°C, has a cubic symmetry with a lattice constant smaller than the substrate. When cooling through the phase transition at ca. 60°C, domains with the c-direction in the film plane are favoured because the spontaneous expansion compensates the strain. The poling of the films with co-planar electrodes eliminates most domain walls parallel to the field resulting in films with domain structure as schematically shown in Fig. 1. This alternating domain structure satisfies an average lattice matching, $(a+c)_{\text{film}}=2a_{\text{substrate}}$.

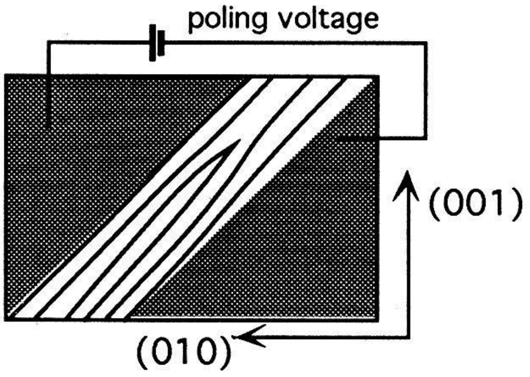

Fig. 1 Configuration of the poling electrodes and schematic sketch of the resulting domain walls. The spontaneous polarisation direction alternates between the [010] and the [001] direction as one moves from one to the next domain. The domains are up to 1 mm long and about 2 µm in diameter. The domain walls are along the (011) planes.

The poling was done at 65°C with an applied field of E_{dc}=1kV/cm. The pyroelectric response was investigated with the method described by Ref. [4]. The chopped laser beam had a wavelength of 632nm and an average power of 2.5 mW which was absorbed by a thin layer of dried ink on the sample. The voltage drop over a shunt resistor of 1 MΩ was recorded with a lock-in amplifier. The frequency dependence of the pyroelectric signal is shown in Fig. 2. The data around 50 Hz was eliminated because of errors caused by line voltage interference. The capacity of the sample was about 0.2 nF leading to an electrical response time of 0.2 ms. The thermal response time is determined by the film thickness (about 15 µm) and the penetration depth of the thermal wave. The theoretical curve fits the data nicely and explains the overall frequency behaviour. Fig. 3 shows the 200 Hz response as a function of temperature. The signal increases on heating as the transition temperature is approached. When the sample is heated above the transition temperature, the signal must vanish because the pyroelectric effect is not allowed in the cubic phase. As seen from Fig. 3, the signal does not drop sharply indicating a "smeared out phase transition". This can often be observed in crystals of solid solution systems, e.g. KTN or PZT. The maximal signal is observed at 65°C.

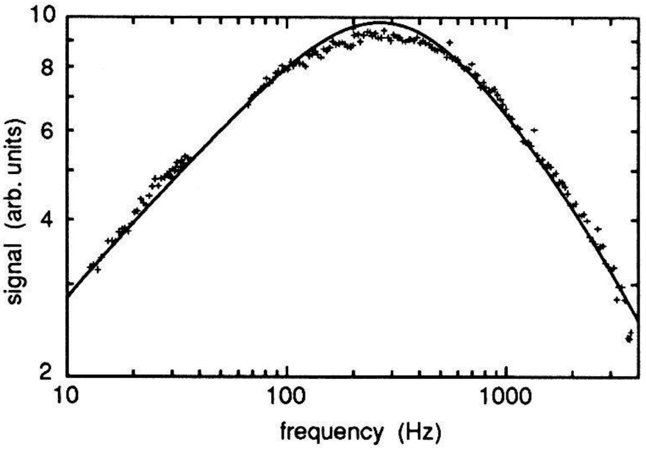

Fig. 2 Frequency dependence of the pyroelectric response at room temperature.

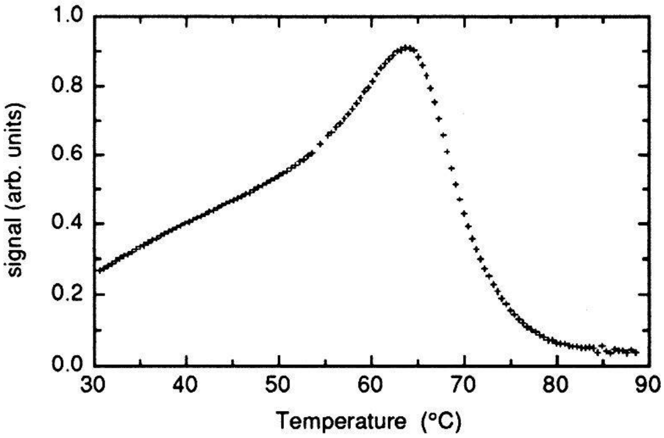

Fig. 3 Temperature dependence of the pyroelectric response at 200 Hz.

References

1. R. Gutmann and J. Hulliger, Cryst. Properties and Preparation **32-34**, 117 (1991).
2. O. M. Stafsudd and M. Y. Pines, J. Opt. Soc. Am. **62**, 1153 (1972).
3. R. Gutmann, J. Hulliger and E. Reusser, J. Cryst. Growth (to be published).
4. H. Vogt, P. Würfel, U. Hetzler and W. Ruppel, Ferroelectrics **33**, 243 (1981).

Blue light second harmonic generation in ion-implanted KNbO3 waveguides

D. Fluck and P. Günter
Institute of Quantum Electronics, Swiss Federal Institute of Technology
ETH Hönggerberg , CH-8093 Zürich, Switzerland.

M. Fleuster and Ch. Buchal
Institut für Schicht- und Ionentechnik
Forschungszentrum Jülich, D-5170 Jülich, Germany.

We report efficient optical frequency doubling from the near infrared into the blue spectral range in ion-implanted $KNbO_3$ planar and channel waveguides. Two configurations have been investigated: (i) guided mode phase-matched and (ii) Cerenkov-type second harmonic generation where the second harmonic is radiated into the substrate. With 176 mW of fundamental power in a channel guide of 5.6 mm length a blue light output power of 7.1 mW is obtained giving a normalized conversion efficiency of 41%/Wcm.

Several approaches have been described for generating blue light by frequency doubling near infrared laser sources in nonlinear optical materials [1]. $KNbO_3$ has been shown to have excellent nonlinear optical properties making it particularly attractive for nonlinear optics [2]. Thanks to its large nonlinear optical susceptibilities, its room-temperature phasematchibility at 860 nm, its transparency down to 390 nm, and its very high threshold to optical damage, $KNbO_3$ proved to be one of the most promising materials for high-efficiency frequency doubling of near infrared laser radiation into the blue and green spectral range [3].

Second harmonic generation (SHG) using optical waveguides is very attractive due to the tight beam confinement over long interaction lengths enabling to achieve high conversion efficiencies even on the power level of presently available diode lasers. Ion implantation and sputter deposition are the only methods so far reported to produce crystalline low-loss optical waveguides in $KNbO_3$ [4-6]. We have reported for the first time phase-matched (PM) and Cerenkov-type SHG in ion-implanted planar and channel $KNbO_3$ waveguides [7,8].

The $KNbO_3$ waveguides used in this work have been produced by using low-dose MeV He ion implantation because for these conditions low-loss planar and channel waveguides have been produced [4,5]. The SHG experiments were performed with a cw titanium sapphire laser with a linewidth of less than 5 GHz. The waveguide input coupling was accomplished with a microscope objective. The mode coupling insertion loss was about 4 dB.

The SH power was measured as a function of the input power for different planar and channel waveguides. We have found that PM SHG was achieved in a mode-to-mode conversion in the planar waveguides whereas in the channel waveguides we observed Cerenkov-type SHG where the blue light is radiated into the substrate.

With a fundamental power of 165 mW in a 5.6 mm long and 5.4 µm thick planar waveguide a power of 2.4 mW of SH blue light at 433 nm was generated, which is equivalent to a normalized conversion efficiency of 16 %/Wcm. The mode conversion was between the TM_0 mode and the TE_1 mode of the planar waveguide.

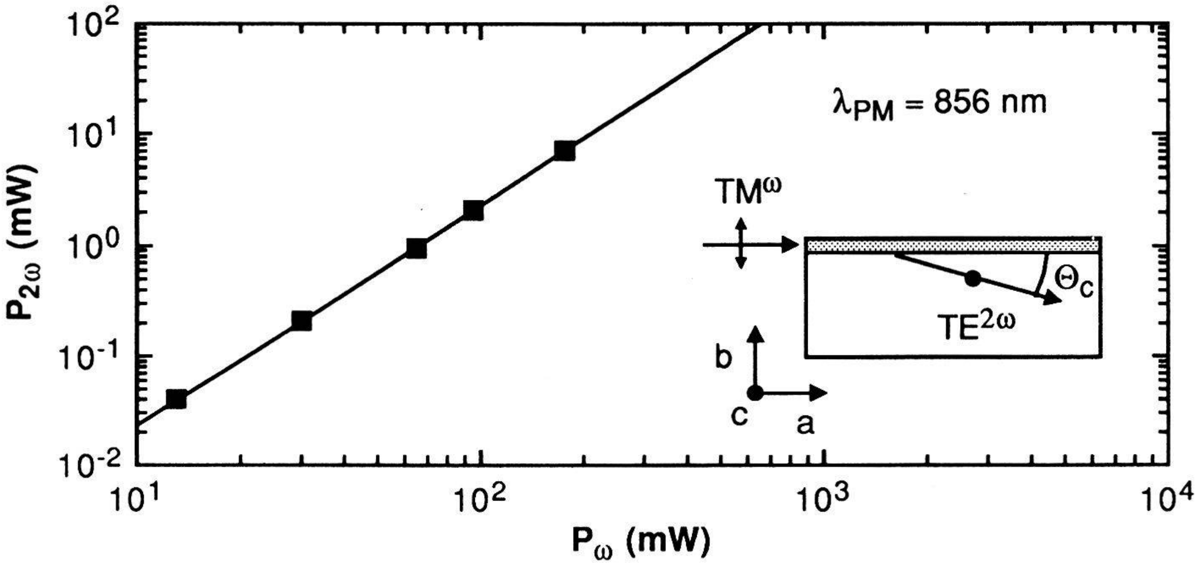

Figure 1: Power of the SH as a function of the fundamental power for Cerenkov-type frequency doubling in an ion-implanted $KNbO_3$ channel waveguide.

A maximum power of 176 mW at 856 nm was coupled into a 5.4 µm x 7.5 µm channel waveguide of 5.6 mm length generating a blue light output power of 7.1 mW at 428 nm. Figure 1 shows the SH power at 428 nm measured as a function of the fundamental power. The theoretical curve corresponds to a normalized conversion efficiency of 41 %/Wcm. The SH radiation was emitted under a Cerenkov angle Θ_c of less than 5 degrees into the bulk crystal.

Based on these results we estimate that 15 mW of blue light can be generated from 100 mW input power using carefully optimized $KNbO_3$ waveguides of 1 cm length.

References

[1] e. g. G. I. Stegeman and C. T. Seaton, J. Appl. Phys. **58**, R57 (1985).
[2] P. Günter, Appl. Phys. Lett. **34**, 650 (1979).
[3] J.-C. Baumert, P. Günter, and H. Melchior, Opt. Commun. **48**, 215 (1983).
[4] F. P. Strohkendl, P. Günter, Ch. Buchal, and R. Irmscher, J. Appl. Phys. **69**, 84 (1991).
[5] D. Fluck, M. Fleuster, Ch. Buchal, and P. Günter, J. Appl. Phys. **72**, 1671 (1992).
[6] S. Schwyn Thöny, P. Günter, and H. W. Lehmann, Appl. Phys. Lett. **61**, 373 (1992).
[7] D. Fluck, B. Binder, M. Küpfer, H. Looser, Ch. Buchal, and P. Günter, Opt. Commun. **90**, 304 (1992).
[8] D. Fluck, J. Moll, M. Fleuster, Ch. Buchal, and P. Günter, Electron. Lett. **28**, 1092 (1992).

THERMAL CONTROL OF AN ULTRASONIC RESONATOR

O. OEHLER, S. MEIER, D. LUTZINGER and J. WIELAND
Institute for Quantum Electronics,
Swiss Federal Institute of Technology, CH-8093 Zurich, Switzerland.

The thermal tuning of an ultrasonic resonator makes the selective detection of gases via the photothermal effect possible. A separation of the tuning control of the resonator, consisting of two facing transducers, from the signal to be measured is possible because of the large difference between the period of the heat source and the thermal time constant of the device.

The temperature dependence of the velocity of sound offers possibilities for the construction of a micro-calorimeter. It is based on the temperature induced detuning of ultrasonic resonators. Such a device can be used for measuring the heat which is produced on the absorption of infrared radiation by gases. This photothermal method is less sensitive than the photoacoustic effect which measures the acoustic signal produced by the light absorbing gas [1]. However, while the photothermal signal can be obtained in a flow system, a photoacoustic cell usualy has to be closed during the measuremenmt.

In earlier work the thermal detuning of the ultrasonic resonator by a periodically heated sample was achieved by varying the distance between two facing ultrasonic transducers. For this purpose one of the transducers was fixed to a piezo-driven actuator [2]. Such an actuator suffers from both the complexity of the device and from the need for a high driving voltage. The replacement of the mechanical tuning by the thermal one was therefore considered. This solution was suggested by former investigations on a thermistor-controlled thermostated resonator housing [3].

The resonator cavity C consists of two identical transducers arranged opposite each other and at a distance of about 6 mm in an thermally isolated (I) metal tube T (Fig. 1). The transducers (one used as an emitter E, the other as a receiver R) were tuned to an acoustic resonance at a frequency of 220 kHz (Z). The phase of the received signal was compared (F) to the input signal. A signal proportional to the phase difference was used to control (U) the temperature of the resonator housing by a Peltier element P.

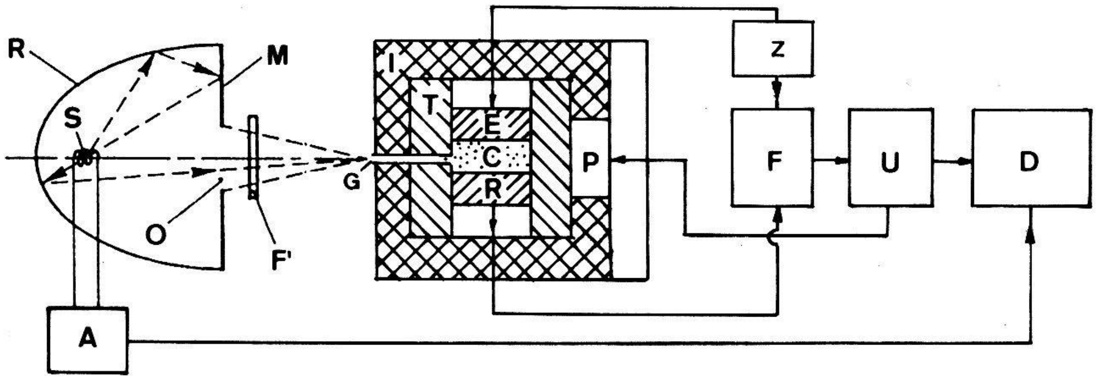

Fig. 1 Ultrasonic resonator, composed of two transducers E and R and a temperature control unit U. Monochromatic and periodic infrared radiation from the source S is fed into the resonator by a wave guide G.

In order to measure (D) the infrared absorption of a gas, the intensity modulated (A) radiation of the thermal light source S was guided into the resonator after passing a filter F. The light collection was carried out by an elliptical reflector R equipped with a counter-reflecting plane mirror M. This mirror M was attached at the central plane of the two foci of the ellipsoid [4] and allowed the decoupling of a collimated beam through opening O in its center.

The gas is fed into the resonator through a piping system whereby the gas temperature has to be adapted carefully to the temperature of the resonator housing.

The thermal controller (U) serves to maintain the operation point of the resonator tuning. Slow drifts may be caused mainly by changes of the velocity of sound due to changes of the gas composition. The absorption induced effects represents small variation arround the operating point.

The need for measuring a small temperature signal by the detuning of the resonator on one hand, and on the other hand for tuning the resonator via the temperature are contradictory. It was found that the thermal time constant of the gas in the resonator is smaller by a factor of 50 (τ = 0.07 sec) than the time constant of the resonator housing (τ = 3.2 sec). It is therefore possible to separate the photothermal signal from the signal controlling the tuning of the resonator.

Fig. 2 shows the dependence of the photothermal signal (see Fig. 3) and the modulated part of the controlling signal as a function of the proportional gain of the controller. It is noticeable that the photothermal signal decreases on an increase of the controlling gain while the controlling signal fed to the Peltier element is increasingly modulated by the photothermal effect.

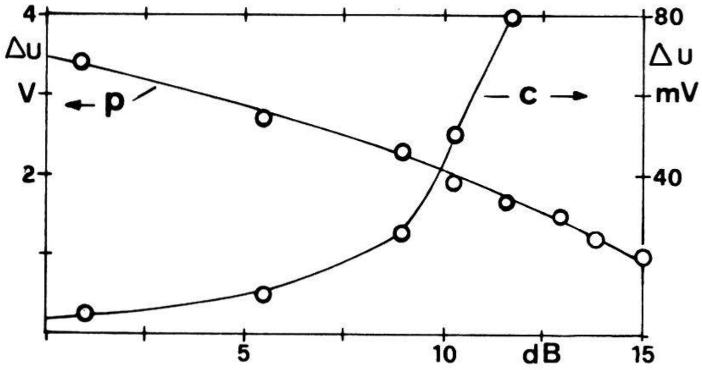

Fig.2 Dependence of the photothermal (p) and the controlling (c) signal from the proportional gain of the temperature controller.

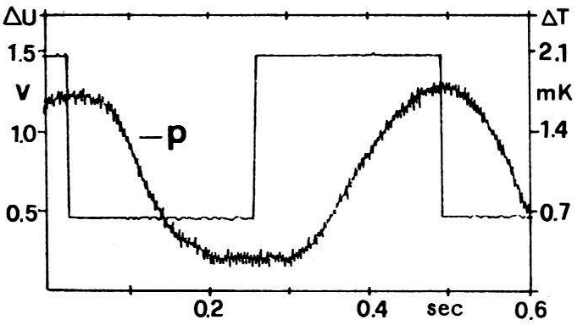

Fig.3 photothermal signal (p) obtained for 500 ppm CO_2 in N_2 with a thermal source (1.8 W electrical power) thermally modulated at 2 Hz.

References

[1] O.Oehler, S.Friedrich and A. Schäppi, Springer Series in Optical Sciences, **62**, Photoacoustic and Photothermal Phenomena II, 519 (1990).

[2] Oehler O., Wieland J., Raillard D. and Schumacher M., Proccedings 3rd Int. Conf. on New Actuators, Bremen, 24-26 June,1992, p. 51.

[3] O.Oehler, P.Rusch and S. Dornbierer, Helv. Phys. Acta, **63**, 533 (1990).

[4] O.Oehler, S.Kunz and J.Wieland, Helv. Phys. Acta, **65**, 834 (1992).

Low-Dimensional Modeling of Taylor-Couette Flow

F. Ohle and H. Eckelmann

Institut für Angewandte Mechanik und Strömungsphysik der Universität,
3400 Göttingen, Bunsenstr. 10, FRG

Time signals of a regular Taylor-Couette flow (homoclinic dynamics at $Re = 120$) are represented as a trajectory in a three-dimensional state space. From this representation a low-dimensional system of ordinary differential equation of 3^{rd} order is derived, which is then used as a model for the description of the temporal dynamics.

In recent years progress has been made in describing hydrodynamical systems by using dynamical system approaches. Althought these systems have an infinite number of degrees of freedom, it has been shown, both experimentally and theoretically, that closed- and open-flow systems can possess low-dimensional attractors [1]. Unfortunately, thus far for most hydrodynamical systems a simple low-dimensional model cannot be derived from first principles (i.e. from the Navier-Stokes equations). One way to overcome this problem is to represent the dynamics by a state space reconstruction. If the trajectories have no double points in the state space, an autonomous system of ordinary differential equations can be derived, which then defines an approximate model for the temporal dynamics of the experimental system [2]. Although not obtained from first principles, such a model can be used to predict the system behaviour or to direct a system to a pre-selected or goal dynamics. If a theoretical model is available, in additon, a comparison with the low-dimensional model might be possible [3].

In this note the dynamics of the viscous fluid flow in the gap between two concentric rotating cylinders, known as Taylor-Couette flow is investigated. In the standard system used here, the inner cylinder rotates while the outer cylinder and the two end plates are fixed. (For more datails see Mullin [4].) If in the experiment the Reynolds number ($Re = \omega r_i d/\nu$, ω : rotational frequency of the inner cylinder of radius r_i, d : gap width, and ν : kinematic viscosity) is increased from zero, cells appear in a very narrow range of Re. Since the first study by Taylor [5], because of the large variety of dynamical states and their bifurcation phenomena, this dynamical system has become a very interesting subject for investigations by chaos-theory.

In the following, a low-dimensional ordinary differential equation will be derived from a measured time signal of a standard Taylor-Couette flow at $Re = 120$. The time signal used was measured by laser-Doppler-velocimetry (LDV) at one local point in space. This measurement was made by Dr. Mullin at Oxford University [6]. To construct a differential equation from these data, a method developed by Cremers and Hübler [2] is applied. More details of the construction procedure can be obtained from Ref. [1]. The investigated trajectory of the regular state at $Re = 120$ is shown in Fig. 1 (left). The state space used is defined by the instantaneous velocity component U and its first two time derivatives $V = dU/dt$, and $W = d^2U/dt^2$, and the corresponding values of $U(t)$, $V(t)$, and $W(t)$ have been normalized in the interval $[-1,+1]$. From this representation a low-dimensional model of the type

$$\dot{U} = \frac{dU}{dt} = V, \qquad \dot{V} = \frac{dV}{dt} = W, \qquad \dot{W} = \frac{dW}{dt} = \sum_{\substack{i=0,\ldots,3\\ j=0,\ldots,3-i\\ k=0,\ldots,3-i-j}} a_{ijk} U^i V^j W^k \qquad (1)$$

is constructed, where the a_{ijk} denote the coefficients of the Taylor series expansion. The simulated trajectory from Eq. (1) is shown in Fig. 1 (right). The qualitative agreement between experimental and simulated dynamics is evident. In addition, both representations have only one fixpoint at $U \approx -0.72$. Furthermore, this model produces a similar behaviour, like the weak stability and different kinds of dynamical states in a small parameter range [7]. In the future, it would be of great interest to determine, for different aspect ratios $\Gamma = l/d$ of the gap (l : length of the cylinders), the coefficients a_{ijk} of Eq. (1) for dynamical states in a narrow Reynolds number range, where cells are observed. From these investigations a better physical interpretation of Eq. (1), i.e. an understanding of the physics and dynamics of Taylor-Couette flow, can be expected. Although, a strong conection between the Navier-Stokes equations and the constructed model has not been established yet, it should be possible to predict from Eq. (1) the transition to turbulence, via a stability analysis. Investigations along these lines are in progress.

We acknowledge the many discussions we have had with Dr. T. Mullin and are greatful to him for providing us with the experimental data.

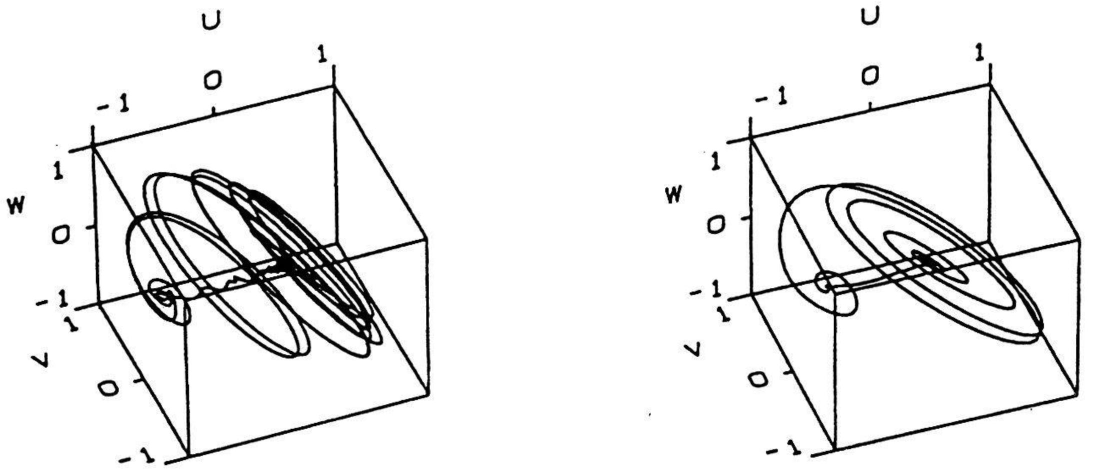

Fig. 1 State space representation of the experimental trajectory (left) and simulated trajectory from the model (right)

References

[1] F. Ohle and H. Eckelmann, Phys. Fluids A **4**, 1702, (1992)
[2] A.J. Cremers and A. Hübler, Naturwissenschaften, **76**, 67, (1989)
[3] B.R. Noack, F. Ohle and H. Eckelmann, Physica D, **56**, 389, (1992)
[4] T. Mullin, IMA J. Appl. Math. **40**, 1, (1990)
[5] G.I. Taylor, Phil. Trans. R. Soc. A **223**, 289, (1923)
[6] T. Mullin, private communications
[7] F. Ohle, MPI für Strömungsforschung, Report Nr. 17/1992, (1992)

ASSESSMENT OF SIMULTANEOUS LIPIDS SUPPRESSION AND LACTATE EDITION ON A WHOLE BODY MRI SYSTEM

Emile M.Hiltbrand*, Tiziano Binzoni*, Graeme McKinnon**
*Département de Radiologie, Hôpital Cantonal Université de Genève
**Département de Radiologie, Universitat Spital, Zurich

For biomedical studies, proton NMR spectroscopy is an important tool which makes it possible to measure in vivo relative concentrations of metabolites, in a non-invasive way. Unfortunately, the proton spectra contains many overlapping lines which makes difficult to consistently assign a line to a particular metabolite. In particular, the lactate and the fat produce lines at the same position on the spectrum. In order to separate the contribution of each one, we have implemented on a whole body Magnetic Resonance Imaging system, a multiple-quantum editing filter, a technique extensively used by the chemists in conventional spectroscopy systems.

Lactate, as an end product of the anaerobic glucose metabolism is an ideal marker of the muscular bioenergetics and it has received a special attention among Nuclear Magnetic Resonance (NMR) spectroscopists for its possible human application on commercially available Magnetic Resonance Imaging (MRI) systems. This application was hampered by the fact that on biological samples, water and lipids are at molar (M) concentrations where metabolites like lactate are measured in millimolar (mM). Consequently, for in vivo studies, the first requirement is to remove the overwhelming contribution of the water protons, and simultaneously to get rid of those lipids protons (-CH2) having a line at the same position as the lactate line. This last step is a far more complicated task than water suppression and requires a careful evaluation on a phantom to assess the efficiency of the editing technique. Several authors claimed having been able to detect lactate without demonstration of this efficiency, consequentely their findings are questionable as it appears that even under moderate ischemia, if some amount of lactate is produced it goes with simultaneous production of mobile lipids. We have shown elsewhere[1] how misleading it can be to assign to lactate the peak showing up at about 1.3 ppm (Tetra Methyl Silane as a reference).

We have designed several Double-Quantum sequences[2,3] but the EDQF compared to a standard Double-Quantum Filter [DQF] noticeably improves the suppression of those mobile lipids produced in some physiological situations like moderate ischemia[4]. It is nevertheless beyond the capability of this phantom model to detect those mobile lipids at the lactate position. (EDQF) sequence takes advantage of the gradients capability on MRI systems, to filter the double quantum transition editing the metabolite of interest directly without any substraction or phase cycling scheme. Because most of the techniques used for in vivo spectroscopy heavily rely on phase, it is crucial to control carefully all effects disturbing this phase containing the information we want. Experiments have shown that our sequence is robust and insensitive to those perturbations.

It turns out that for in vivo experiments, where fat is always present, a prerequisite before assigning to lactate the peak observed at 1.3 ppm is to demonstrate the effectiveness of the fat suppression on a dedicated phantom. Let us briefly describe the protocol we used for this assessment. In a bottle containing oil we inserted a small NMR tube (4mm i.d.) filled with a solution of 5 mM of lactate in isotonic liquid. These 5 mM have to be understood as the actual concentration on the localized volume. We performed three experiments :

1. On the phantom above described and using the sequence to edit the lactate (EDQF) we collected a spectrum from a region where both moieties are present. Because the sequence was designed to suppress the lipids, we assume that the peak observed is due to the lactate only (Figure 1). We then removed the NMR tube and repeated the sequence on the oil alone. Fat is well removed since only noise is seen at 1.3 ppm,(figure 2).

2. Next, we repeated the experiment on excised organs of animals, a more realistic phantom, since it is well established that tissues deprived of oxygenated blood produce lactate. Figure 3 shows a spectrum obtained on a bovine dorsalis muscle where lactate can be seen with EDQF. Chemical analysis has given a lactate content of about 25 mM, a value well within the range of what is achieved in vivo, under ischemia or exercise.

3. On figure 4 are reported five spectra obtained in vivo on a human calf muscle with the standard DQF. The spectrum at the bottom is the reference, (muscle at rest, before the experiment starts). Each of the four remaining proton spectra result from 128 acquisitions (128 NEX) and were collected during moderate ischemia (tourniquet) at a repeat time (TR) equal to 1500 ms. A line at 1.3 ppm might be attributed to lactate but the EDQF sequence repeated under the same protocol did not show any line at 1.3 ppm A simultaneous and interleaved collection of phosphorus spectra (31P) are not showing a shift of the inorganic Phosphorus (Pi) indicating a pH variation concomitant with the production of lactic acid and makes our findings consistent.

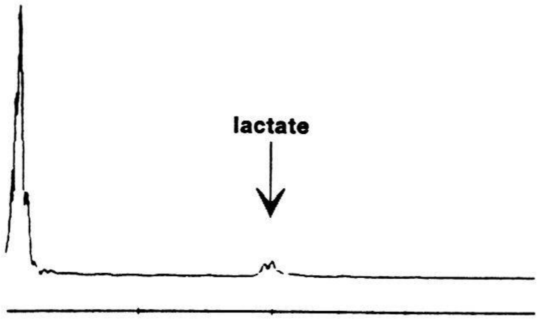

Figure 1

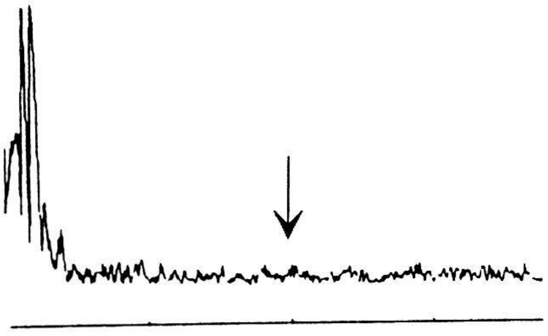

Figure 2

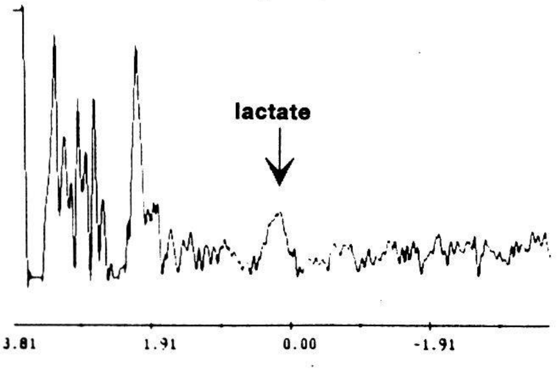

Figure 3

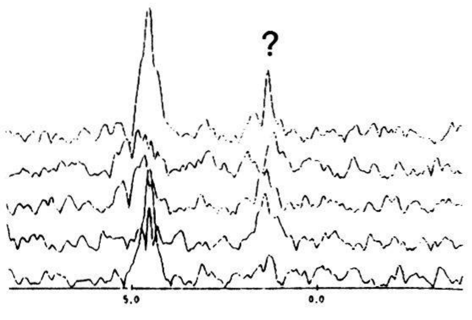

Figure 4

References :
1) E.Hiltbrand et al, Book of abstracts, Soc.Magn.Res. Med, 1228, (1990)
2) G. McKinnon et al., Book of abstracts, Soc.Magn.Res. Med, 222, (1989)
3) J.E. van Dijk et al. NMR in Biomed. **5**, 75, (1992)
4) W.T. Evanochko et al. Magn. Res. Med. **5**, 23, (1987)

RELATIVISTIC CORRECTIONS TO THE SCHRÖDINGER EQUATION DEDUCED FROM THE QUANTUM FIELD THEORY

Etienne FROCHAUX, Département de Mathématiques, EPFL, 1015 Lausanne, Suisse

The problem of the relativistic corrections to the Schrödinger equation began in the 1930's with the Klein-Gordon-Schrödinger and Dirac equations. But to reproduce the experimental measurements, especially the hyperfine structure of the hydrogen atom, it has been necessary to construct a much more complicated theory, the Quantum Field Theory (Q.F.T.). The main difficulty in such a theory is that a given state does not generally describe a well defined number of particles.

The existence of bound states in Q.F.T can be obtained by inspecting an equation, called the Bethe-Salpeter equation. This is a powerful method to prove the existence of such states, but the effective calculations of the bound state masses or the binding energies, by the Bethe-Salpeter equation, are very difficult, even perturbatively. So we try to establish a different method, of a variational type, which presents also the interest of giving new insight into the problem of how particles can be recognized in Q.F.T.

The effective calculations are made in the simplest Q.F.T. models for which the existence of a bound state is known (by the Bethe-Salpeter method), the weakly coupled $P(\varphi)_2$ models. These models have also the advantage of being constructed mathematically rigorously [1]. They describe a quantum and relativistic world populated with one sort of massive and spinless particles, moving in a 2-dimensional space-time and with weak mutual interaction.

The bound state mass m_B is defined by the spectrum of the mass operator M:

$$m_B^2 = \inf_{\psi \neq 0, \psi \in \mathcal{V}} \frac{\langle \psi; M^2 \psi \rangle}{\langle \psi; \psi \rangle}$$

where $\langle \ldots \rangle$ means the scalar product of the state space $\mathcal{H}$ and $\mathcal{V}$ is the intersection of the domain of M and the subspace orthogonal to the vacuum and the one-particle states.

We use a result of the Bethe-Salpeter method, stating that m_B, when it exists, is a C^∞ function of the coupling constant λ, which allows us a perturbative approach.

The variational problems are embarrassed by the use of too many variables. In fact we can restrict ourselves to the zero-time subspace $\mathcal{D}_0$. We cannot proof that $\mathcal{D}_0$ is dense in $\mathcal{H}$, but we have established the weaker (but sufficient for us) statement : for all $\psi \in \mathcal{H}$ and all $N \in \mathbb{N}$ there exists $\eta \in \mathcal{D}_0$ such that $\psi - \eta$ is of order $O(\lambda^N)$.

Our method begins by constructing one-particle states $\chi(f)$ in $\mathcal{D}_0$, for $f \in \mathcal{S}(\mathbb{R}^2)$. Then we define tensorial products $\chi^n(f_1 \otimes \cdots \otimes f_n) = \chi(f_1) \otimes \cdots \otimes \chi(f_n)$ for all n. The most general vector we have to consider is $\chi^2(f) + \lambda \sum_{n \geq 0} \chi^n(f_n^1) + \ldots + \lambda^N \sum_{n \geq 0} \chi^n(f_n^N)$ for some N. It is orthogonal to the vacuum and the one-particle states at $O(\lambda^{N+1})$ by a good choice of the numbers $\{f_0^i\}$ and the functions $\{f_1^j\}$. Our minimization problem becomes

$$m_B^2 = \inf_{f, \{f_m^1\}, \{f_m^2\}, \ldots} \frac{\langle f; M^2 f \rangle + \lambda 2 \Re e \sum_m \langle f; M^2 f_m^1 \rangle + \lambda^2 \sum_{m,n} \langle f_m^1; M^2 f_n^1 \rangle + \ldots}{\langle f; f \rangle + \lambda 2 \Re e \sum_m \langle f; f_m^1 \rangle + \lambda^2 \sum_{m,n} \langle f_m^1; f_n^1 \rangle + \ldots} + O(\lambda^{N+1})$$

(with an obvious notation for the scalar products). The minimization of the λ^0-term by varying f gives $4m^2$, but the minimum is not attained by any function f (the free theory has no bound state!). Moreover f depends on λ in a singular way because we must have

$\langle f; M^2 f\rangle / \langle f; f\rangle = 4m^2 + O(\lambda)$, which we call the *condition for low relative energy.* So we begin the minimization by varying the functions $\{f_m^1\}$. This programme leads to well defined functions $\{f_m^1(f)\}$ (which depend on f), and we are left with the equation, to first orders :

$$\begin{aligned} m_B^2 \; = \; \inf_{0\neq f} \; & \frac{1}{\int d\sigma(p)\,|\,f(p)\,|^2} \Big[\int d\sigma(p)\,|\,f(p)\,|^2\, \mathcal{M}(p)^2 \, + \\ & + \int d\sigma(p)\, d\sigma(p')\, \overline{f(p)}\, f(p')\, \mathcal{B}_1(p,p')\, \delta(p_1 + p_2 - p_1' - p_2') \Big] + O(\lambda^3) \end{aligned}$$

where $d\sigma(p) = dp_1\, dp_2 / 2\omega(p_1) 2\omega(p_2)$, $\omega(p_i) = \sqrt{p_i^2 + m^2}$ for $i \in \{1,2\}$, $\mathcal{M}(p)^2 = (\omega(p_1) + \omega(p_2))^2 - (p_1 + p_2)^2$, and $\mathcal{B}_1(p,p')$ is related to the Bethe-Salpeter kernel [2]. We can repeat these operations by varying the functions $\{f_n^2\}$,..., $\{f_n^N\}$, which leads to well defined functions (depending on f), and the result is simply to replace $\mathcal{B}_1$ by a new kernel $\mathcal{B}$. Our equation can be written as an eigenvalue equation

$$\mathcal{M}(p)^2 f(p) \; + \; \int_{\mathbb{R}^2} d\sigma(p')\, f(p')\, \mathcal{B}(p,p')\, \delta(p_1 + p_2 - p_1' - p_2') \; = \; (m_B^2 + O(\lambda^{N+1}))\, f(p).$$

The separation into a center of mass system and a relative system is not possible. To simplify the equation, all we can do is to write it in the center of mass frame, which gives

$$4p^2 g(p) \; + \; \int_{\mathbb{R}} \frac{dp'}{4p'^2 + 4m^2}\, g(p')\, b(p,p') \; = \; (m_B^2 - 4m^2 + O(\lambda^{N+1}))\, g(p)$$

where $g(p) = f(p,-p)$ and $b(p,p') = \mathcal{B}(p,-p,p',-p')$. Explicit calculations of m_B have been done to first orders and they agree with the results of the Bethe-Salpeter method [2]. We have obtained a two-particle equation for the bound state deduced from the Q.F.T. The difference between our approach and the Klein-Gordon-Schrödinger or Dirac theory is that our equation, obtained by minimization, is valid only for finding the lowest bound state. To find other states we should go back to the space $\mathcal{H}$ and repeat the minimization after orthogonalization with respect to the ground state eigenspace. We would probably obtain also a two-particle equation, but with an other interaction kernel $\mathcal{B}$.

We can illustrate the situation by giving the non-relativistic limit of our calculations (by taking the perturbation expansion in $1/c$ of all terms, where c is the speed of light). We obtain a model of the following type (simplified for a shorter exposition), to first orders. The state space is $L^2(\mathbb{R}^2) \oplus L^2(\mathbb{R}^4)$ and the Hamiltonian is a 2×2 matrix

$$H = \begin{pmatrix} H^{2,2} & H^{2,4} \\ H^{4,2} & H^{4,4} \end{pmatrix} = \begin{pmatrix} 2m/\varepsilon + H_0^{2,2} + \varepsilon H_1^{2,2} + \varepsilon^2 ... & H_0^{2,4} + \varepsilon ... \\ H_0^{4,2} + \varepsilon ... & 4m/\varepsilon + H_0^{4,4} + \varepsilon ... \end{pmatrix}$$

where ε is a small parameter which measures the relativistic effects. The mixing terms $H^{2,4}$ and $H^{4,2}$ are absent in the Klein-Gordon-Schrödinger or Dirac theory, but are imposed by the Q.F.T. The search for the minimum of H leads at first order (ε^0) to the ordinary two-particle Schrödinger equation and at second order (ε^1) to two coupled equations between the two particles and four virtual particles [3].

References: [1] J. Glimm, A. Jaffe, *Quantum Physics*, Second edition, Springer Verlag (1987). [2] E. Frochaux, *The bound states of the weakly-coupled* $\mathcal{P}(\varphi)_2$ *models*, to appear in Nucl. Phys. B. [3] E. Frochaux, A.-M. Moix, C. Raharinosy, *A quantum relativistic model for two interacting particles at zero-time*, in preparation.

Scaling Law and Pruning in 2D Maps

J. Vollmer, and W. Breymann
Inst. für Physik, Universität Basel, 4056 Basel, Switzerland

We investigate the invariant set of a family of twodimensional maps with constant Lyapunov exponents. Their behaviour is described by a symbolic dynamics that becomes incomplete at a critical parameter value (pruning). At the critical point the topological entropy of the invariant set starts to decrease with a power law. Its exponent is calculated analytically by scaling arguments.

Two-dimensional, piecewise linear, area-preserving maps with constant Lyapunov exponents describe scattering problems in billiards with gravitation [1] and allow to calculate the number of metastable states of nonlinear chains with piecewise harmonic interactions [2]. Furthermore they form the simplest class of systems that show pruning as it was firstly discussed for Hénon-type maps [3]. The former systems are described by Baker-transformation-like maps of the plain onto itself:

$$\mathcal{F} : \begin{pmatrix} x_n \\ y_n \end{pmatrix} \mapsto \begin{pmatrix} x_{n+1} \\ y_{n+1} \end{pmatrix} = \begin{cases} \begin{pmatrix} \eta^{-1}\, x_n \\ \eta\, y_n \end{pmatrix}, & \text{for } y_n < \frac{1}{2}\,(1+\eta) - \eta\, x_n \\ \begin{pmatrix} 1-\eta^{-1}\,(1-x_n) \\ 1-\eta\,(1-y_n) \end{pmatrix}, & \text{for } y_n > \frac{1}{2}\,(1+\eta) - \eta\, x_n \end{cases} \tag{1}$$

where x_n and y_n are related to the original problem by $x_n = (1-\eta)\sum_{j=0}^{\infty} \eta^j s_{n+j+1}$, $y_n = (1-\eta)\sum_{j=0}^{\infty} \eta^j s_{n-j}$ and $s_n = \Theta\,(X_n - \text{const})$. Here X_n denotes x-coordinates of scattering events in the billiard and particle distances for the anharmonic chain, respectively, and $\Theta\,(x)$ is the Heavyside-function. The Lyapunov exponents of the system are $\pm\ln(\eta)$, and variables are scaled in such a way that the points $(0,0)$ and $(1,1)$ are (hyperbolic) fixed points of eq. (1). Therefore all points of the invariant set lie within a Cantor set with scaling η in the unit square. Any point in this set represents a physical state as long as the set does

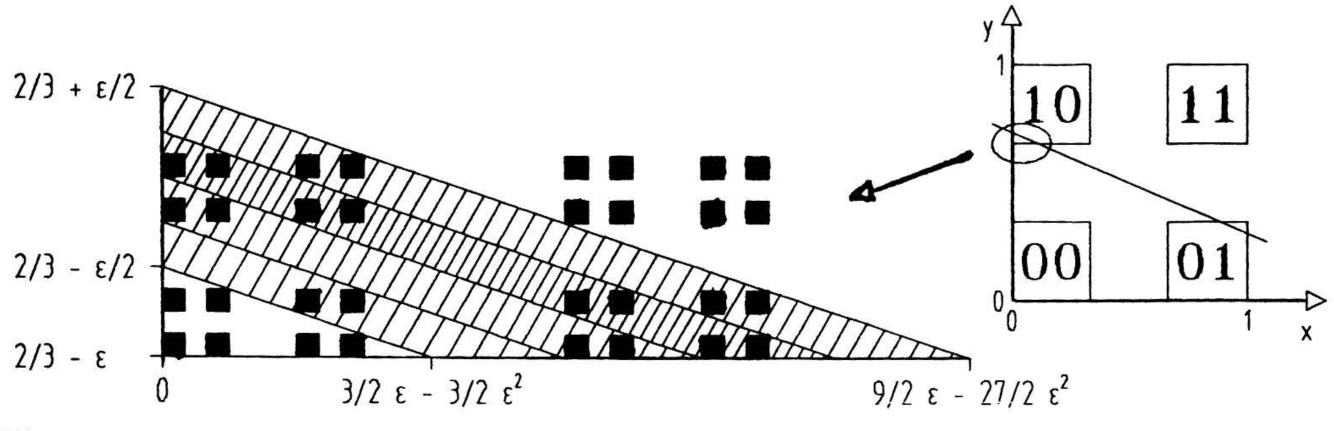

Figure 1: Close-up of the triangle firstly cut out by the critical line $y = 1/2\,(1+\eta) - \eta\, x$. Note that the pattern repeats when changing ϵ by factors of 3 and that differently hatched strips contain different numbers of boxes.

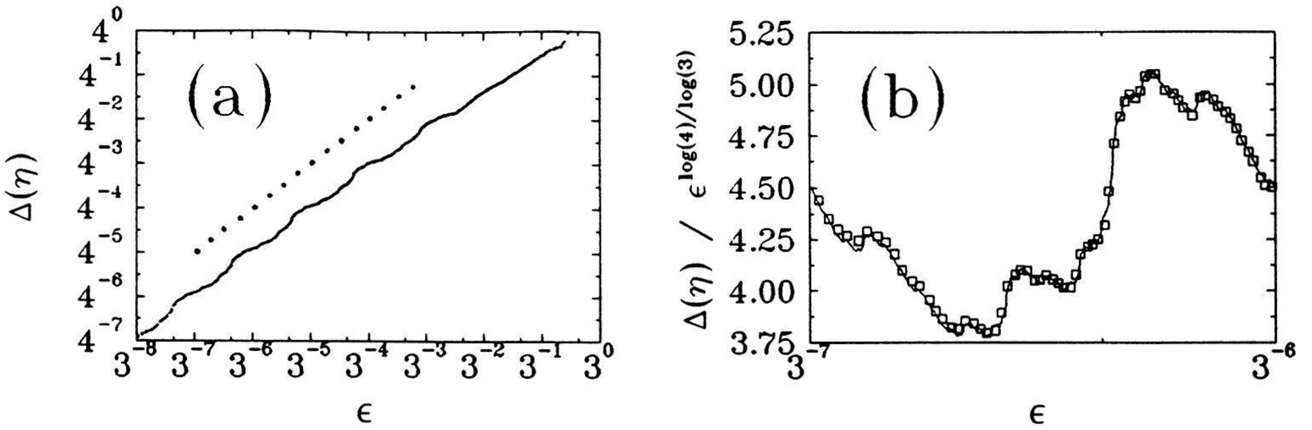

Figure 2: Comparison between the analytic result for the topological entropy K_0 and numerical data from ref. [4]. (a) Deviation of K_0 from ln 4. The dotted line corresponds to a power-law with slope $\log 4/\log 3$. (b) Deviation of K_0 from power law behavior. Note that the proportionality constant (cf. eq. (2)) is only fixed by the numerical data (open squares).

not intersect with the critical line $y = (1+\eta)/2 - \eta x$, i. e. for $\eta < \eta_c \equiv 1/3$. Otherwise points that are mapped into one of the triangles cut out in the upper left and lower right square, respectively, become forbidden (cf. fig 1). As a consequence the symbolic dynamics becomes incomplete and the topological entropy $K_0(\eta)$ of the invariant set starts to decrease from its former value ln 4, i. e., the system shows pruning. The deviation is measured by $\Delta(\epsilon) \equiv 1 - K_0(\eta_c + \epsilon)/\ln 4$.

The onset of pruning is governed by a scaling law, as can be seen from fig. 1. This allows to calculate $K_0(\eta = \eta_c + \epsilon)$ by noticing that the number $f_N(\epsilon)$ of forbidden orbits on the Nth level of the fractal and at parameter value ϵ is related to f_{N+1} by $f_N(\epsilon) = f_{N+1}(\epsilon/3)$ and consequently

$$\Delta(\epsilon) \sim \lim_{N\to\infty} \frac{1}{N}\frac{f_N(\epsilon)}{4^N} \sim 4\,\Delta\left(\frac{\epsilon}{3}\right) \quad \Rightarrow \quad \Delta(\epsilon) \sim \epsilon^{\log 4/\log 3}\,. \tag{2}$$

There is fine structure on the scaling that can be generated by box counting in fig. 1. Taking three times finer strips at any level of the fractal, histograms of successive N are related by a recursion relation. The values for $\Delta(\epsilon)$ calculated from these histograms agree with numerical data from [4] up to an error less than 1% (cf. fig. 2).

Note that ϵ measures the size of the triangles cut out, and $D \equiv \log 4 / \log 3$ is the fractal dimension of the unpruned set. Therefore we conjecture that the relation $\Delta(\epsilon) \sim \epsilon^D$ also holds in other systems, but—of course—with different fine structure.

The authors like to thank H. Thomas and R. Schilling for valuable discussions and remarks. This work was supported in part by the Swiss National Science Foundation.

References

[1] M. Hénon, Physica **D33**, 132–156 (1988).
[2] P. Reichert and R. Schilling, Phys. Rev. **B32**, 5731 (1985).
[3] P. Cvitanović, et. al., Phys. Rev. **A38**, 1503 (1988).
[4] J. Vollmer, W. Breymann and R. Schilling, submitted to Phys. Rev. **B**.

New Analogies between the Noisy Feigenbaum Scenario and Critical Phenomena

P. Reimann and P. Talkner

Paul Scherrer Institut, CH-5232 Villigen and
Institut für Physik, Klingelbergstr. 82, CH-4056 Basel

The concepts of universality and scaling play an important role in various fields of theoretical physics like e.g. critical phenomena, nonlinear dynamics, hydrodynamics etc. [1]. In this note we work out further striking analogies of the the Feigenbaum route to chaos [2] in presence of weak noise [3,4] to the theory of critical phenomena.

The noisy Feigenbaum scenario is described by the one-dimensional Langevin equation for the dynamical variable x in discrete time n [3,4]

$$x_{n+1} = f_\mu(x_n) + g_\mu(x_n)\xi_n \tag{1}$$

where $f_\mu(x)$ is a map with an invariant interval I_μ with negative Schwarzian derivative [2] smoothly depending on the control parameter μ and on x with the possible exception $x = 0 \in I_\mu$ where the map has its global maximum of of order $z > 1$. The noise coupling function $g_\mu(x)$ is required to be smooth, positive, and bounded. The distribution of the uncorrelated random numbers ξ_n is given by

$$P_a(\xi_n) = u_a(\xi_n)\exp\{-h_a(\xi_n)/\sigma^a\} \tag{2}$$

where the small parameter σ determines the noise strength, the prefactor $u_a(\xi_n)$ is smooth, positive and bounded, and the exponentially leading part $h_a(\xi_n)$ has a global minimum of order $a > 0$ at $\xi_n = 0$ and is smooth everywhere else.

Iteration of (1) leads to the renormalization group transformation that can be formulated in terms of the deterministic renormalization operator [3,4] $(\hat{T}f_\mu)(x) := -\alpha f_\mu(f_\mu(-x/\alpha))$. Using an appropriate parametrization of μ and x one obtains [2]

$$(\hat{T}^k f_{\mu/\delta^k})(x) \to f^*_\mu(x) \tag{3}$$

for $k \to \infty$, $x \in I^*_\mu$. Here α and δ are the universal Feigenbaum numbers and the maps $f^*_\mu(x)$ constitute the unstable invariant manifold of the operator $\hat{T}$. For the full renormalization group this manifold yields one relevant direction in function space at the critical point $f^*_{\mu=0}(x)$. Similarly the scaling limit $g^*_\mu(x)$ of the noise coupling functions gives another relevant direction.

The renormalization group yields an approximate scaling relation for the invariant density $W_{\sigma,\mu}(x)$, $x \in I_\mu$, of the stochastic process (1) [5-7]

$$\alpha\, W_{\sigma,\mu}(x) \simeq 2\, W_{\sigma/\kappa,\mu/\delta}(-x/\alpha) \tag{4}$$

where κ is the scaling factor of the noise strength σ. Strict scaling holds only in the trivial case with vanishing noise $\sigma = 0$. However, for the invariant functions $f^*_\mu(x)$, $g^*_\mu(x)$ the deviations from exact scaling become extremely small.

As a further approximative result a Frobenius-Perron-like relation [6]

$$W_{\sigma,\mu}(x) \simeq \sum_{f_\mu(y)=x} W_{\sigma,\mu}(y)\,|f'_\mu(y)|^{-1} \tag{5}$$

is found, valid for such $x \in I_\mu$ for which there exists at least one $y \in I_\mu$ with $f_\mu(y) = x$. For $a \leq 1/2$ (5) is exact in exponentially leading order in σ but not for $a > 1/2$, although it may still yield good approximations.

Using (3)-(5) one recovers the scaling behaviour of the envelope $\bar{\lambda}$ of the Lyapunov exponent $\lambda(\sigma, \mu) = \int W_{\sigma,\mu}(x) \ln |f'_\mu(x)| \, dx$ [3,4]

$$\bar{\lambda}(\sigma, \mu) = |\mu|^{\frac{\ln 2}{\ln \delta}} L(\sigma \, |\mu|^{-\frac{\ln \kappa}{\ln \delta}}) \qquad . \tag{6}$$

where L is a scaling function.

In terms of critical phenomena [8] the noise strength σ can be identified with the relevant scaling field, $\bar{\lambda}$ is then the order parameter, and $\ln \delta$, $\ln \kappa$ are the critical exponents [3,4]. Any further critical exponent can be expressed in terms of $\ln \delta$ and $\ln \kappa$, i.e. we are dealing with a two exponent theory. The Feigenbaum number α must not be confused with a critical exponent. It rather corresponds to the spatial scaling factor in a real space renormalization theory [4]. Eq.(4) corresponds to scaling of the coarse grained partition function and (6) to the equation of state.

The scaling factor δ as well as the Feigenbaum number α depend on z [2] whereas κ depends on both z [9] and a [7] but are independent of further details of (1), (2). Thus the numbers z and a are related to the dimensionality of space and number of components of the order parameter which completely determine the universality class, fixed point and critical exponents [8].

As in (5) fluctuations are no longer taken fully into account this may be considered as the counterpart of mean field approximation for critical phenomena. Within this approximation one finds $\kappa_{MFA} = \alpha^z$ independent of a. This result follows from the full renormalization theory only if $a \leq 1$. Hence, we identify a^{-1} with the dimensionality d of space and find as its critical value $d_c = 1$. For $d < d_c$ the noise scaling factor κ is given by

$$\kappa = \alpha^z (1 + [c(z,d)/\alpha^{z-1}]^{\frac{1}{d_c - d}})^{d_c - d} \tag{7}$$

with $1 > c(z,d) > 0$ having well defined limits $d \to 0$ [7] and $z \to \infty$. Eq.(7) may be read either as $d_c - d$-expansion or as hyperscaling relation. Note that the second scaling factor δ is independent of d.

Finally we note that the whole analysis can be generalize to a large class of correlated noise including Ornstein-Uhlenbeck noise. In particular these systems belong to the same two exponent universality class independent of the correlation of the noise.

References

[1] L.Kadanoff, Physica A **163**, 1, 1990.
[2] P.Collet, J.-P. Eckmann, O.Lanford III, Comm.Math.Phys.**76**, 211, 1980.
[3] J.Crutchfield, M.Nauenberg, J.Rudnick, Phys.Rev.Lett.**46**, 933, 1981.
[4] B.Shraiman, C.Waine, P.Martin, Phys.Rev.Lett.**46**, 935, 1981.
[5] P.Reimann, P.Talkner, Phys.Rev.A **44**, 6348, 1991.
[6] P.Reimann, P.Talkner, Helv.Phys.Acta **64**, 946, 1991.
[7] A.Hamm, R.Graham, J.Stat.Phys.**66**, 689, 1992.
[8] M.Fisher, Lecture Notes in Physics **186**, Springer, 1983.
[9] F.Argoul et al., Europhys.Lett.**3**, 643, 1987.

Renormalization Group Theory of Transport Properties of Disordered Systems

B. Payandeh[1] and M. Robert[1,2]

Rice Quantum Institute, Rice University, Houston, Texas 77251–1892, USA
[1] on leave at Department of Theoretical Physics, University of Geneva, CH–1211 Geneva, Switzerland
[2] on leave at Institute of Theoretical Physics, ETH–Hönggerberg, CH–8093 Zürich, Switzerland

A cluster expansion renormalization group in real space is developed for disordered systems. In contrast to previous approaches, it considers the cluster size distribution (free energy) rather than the site or bound probability distribution (coupling constants), and satisfies the basic renormalization group requirement of free energy conservation. The critical exponents of the percolation model are found to converge to exact values as higher orders in the expansion are considered. The method is applied to the study of the conductivity and elasticity of disordered solids. The predictions for conductivity converge to experimental values, and those for the bond-bending model of elasticity agree well with experimental and computer simulations results.

Much of the current theoretical work on transport in disordered systems uses percolation as the microscopic model to describe disorder, and renormalization group theory has been widely used to study its critical behavior. Unfortunately, all previous attempts to apply renormalization group theory in real space to percolation and transport in disordered systems are open to criticism at the fundamental level, and thus could never be considered satisfactory.

In contrast to the case of a non-disordered system such as the Ising model of a magnet, when the degrees of freedom are local (spin variables attached to a site) and the renormalization group equations are obtained by partially summing the partition function (free energy) over these local degrees of freedom at short distances, for a disordered system such as the percolation model, the free energy involves sums over nonlocal quantities (the size and perimeter of the clusters of nearest-neighbor occupied sites), which span all ranges of the system.

Since the degrees of freedom are the cluster degrees of freedom, the clusters themselves must be considered in the process of constructing the renormalization group equations. An exact mapping is defined between clusters in the original and renormalized systems, and clusters are correspondingly grouped into classes according to their topological structure. Upon renormalization, new types of couplings (connections) are generated in the renormalized system, which alter the topological structure of the clusters as compared to their structure in the original system. In order to preserve the topological structure of the clusters, new couplings must be added in the original system. We will thus have to take into account the contribution from different clusters to each coupling, which provides us with a natural way to classify the clusters. Summation over short-distance degrees of freedom in the original system is performed for the probability distribution of each class of clusters; this yields the probability distribution of the corresponding class of clusters in the renormalized system, leading to the renormalization group equations. The renormalization group transformation is constructed exactly for finite clusters (here in the sense of cluster expansion) and as larger clusters are considered, higher orders of the expansion are obtained.

To illustrate our method, consider the three-cell approximation of the renormalization group transformation for the square lattice. The sites of the lattice are grouped into blocks of edge length $L = 2$. In this case, there are three classes of topologically distinct clusters. The first class contains all clusters with occupied blocks connected by nearest-neighbor couplings. In the second class, diagonal couplings are present, whereas the third class includes clusters with occupied but unconnected blocks.

In the absence of an external field, the renormalization group equations for the probability distributions of the corresponding classes of clusters read:

$$\begin{aligned}
\mathrm{P}_{nn}(p_b, r_b, d_b) &= \mathrm{P}_{nn}(p, r, d), \\
\mathrm{P}_{nnn}(p_b, r_b, d_b) &= \mathrm{P}_{nnn}(p, r, d) \\
\mathrm{P}_{bond}(p_b, r_b, d_b) &= \mathrm{P}_{bond}(p, r, d).
\end{aligned}$$

where P(**P**) is the probability distribution of the different classes of clusters in the original (renormalized system, *nn* and *nnn* stand for nearest-neighbor and nearest-nearest-neighbor, respectively, $p(p_b)$ is the probability that a site (block) is occupied, $r(r_b)$ is the probability that a nearest-neighbor bound exists between two sites (blocks) and $d(d_b)$ is the probability that two next-nearest-neighbor sites (blocks) are connected by a diagonal bond.

The results for the correlation length exponent (the inverse of the thermal exponent) and the fractal dimension (the magnetic exponent) are 1.42, 1.41 and 1.37 and 1.79, 1.81 and 1.86, respectively, for the one-, two- and three-cell approximations. These results compare favorably with the presumed exact values of 1.33 and 1.89.

Finally, the present method has been applied to the study of the conductivity and elasticity of disordered solids [1]. For the conductivity problem, the result for the ratio t/ν, with t the conductivity exponent and ν the correlation length exponent, is 0.98 for the three-cell approximation on the triangular lattice, in excellent agreement with the recent experimental result $t/\nu = 0.98$ [2]. For the bond-bending model of elasticity, we consider the two-cell approximation on a triangular lattice. The result for the critical exponent ratio f/ν, with f describing the vanishing of the elastic moduli at threshold, is $f/\nu = 2.83$, in good agreement with the results 2.7 ± 0.2 of experiment [3] and 2.97 of computer simulations [4].

The authors are grateful to the Departments of Theoretical and Condensed Matter Physics of the University of Geneva and the Department of Physics of the ETH for their generous hospitality.

References

[1] M. Knackstedt, Ph.D. thesis, Rice University (1991).
[2] J.M. Gordon, A. Goldman and B. Whitehead, Phys. Rev. B38, 12019 (1988).
[3] L.C. Allen, B. Golding and W.H. Haemmerle, Phys. Rev., B37, 3710 (1988).
[4] J.C. Zabolitzky, D.J. Bergman and D. Stauffer, J. Stat. Phys. 44, 211 (1986).

Turing Structures in Cellular Automata Models of Reaction-Diffusion Systems

M. Droz and L. Frachebourg

Département de Physique Théorique, Université de Genève,1211 Genève 4

Chemical reactions involving several species are generally described by macroscopic equations for the evolution of the local average densities of the chemicals. This mean-field approximation neglects an important element of the problem, namely the microscopic fluctuations. In order to understand the role of these fluctuations, we define a probabilistic Cellular Automata (CA) model for reaction-diffusion systems taking the fluctuations into account in a natural way. This model captures the essential features of the problem but is simple enough to permit large simulations.

We present here our model and results in two dimensions for a particular autocatalytic reaction called the Schnackenberg reaction, and defined as:

$$\begin{array}{cc} A \xrightarrow{k_1} X & X \xrightarrow{k_2} 0 \\ 2X + Y \xrightarrow{k_3} 3X & B \xrightarrow{k_4} Y\,. \end{array} \tag{1}$$

The corresponding macroscopic rate equations for the local average densities x and y are:

$$\begin{aligned} \partial_t x &= k_1 a - k_2 x + k_3 x^2 y + D_x \nabla^2 x \\ \partial_t y &= k_4 b - k_3 x^2 y + D_y \nabla^2 y\,. \end{aligned} \tag{2}$$

The CA model consists of a multi-species lattice gas [1]. The state of each site is characterized by the occupation number of each species $|n_A(\vec{r},t), n_X(\vec{r},t), n_Y(\vec{r},t), n_B(\vec{r},t) >$ $,(n_i(\vec{r},t) = 0, 1, ...)$. The parallel evolution of the CA is composed of two stages. First the diffusion in which each particle jumps to a nearest neighbour site with an equal probability. Each species can diffuse with its own diffusion constant. Then the reaction stage couples the species together. In this stage, the reactions (1) are explicitly implemented on each site of the lattice. Averaging over all possible configurations, these rules reproduce the macroscopic rate equations in the continuous limit and in a mean-field approximation.

The recent experimental observations [2] of Turing structures [3] in chemical reactions have motivated a renewal of interest for this problem. This is the reason why we have investigated one of the simplest reaction exhibiting such structures. Under certain conditions, reaction-diffusion systems can produce heterogeneous steady state spatial patterns which evolve by diffusion driven instabilities. These patterns are characterized by an intrinsic wavelength independent of the size of the system. The domain of parameters space for which such patterns exist is called the Turing space.

Appropriate choice of the parameters for our CA model leads to the pattern shown in figure 1.

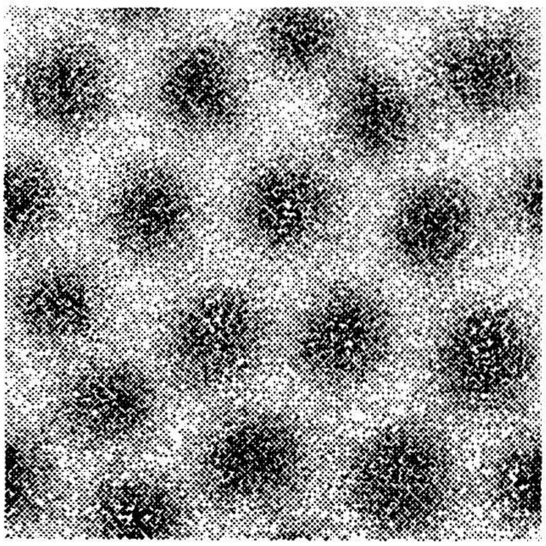

Figure 1: Turing pattern for the concentration of one reactor in CA model of Schnackenberg reactions

Hexagonal patterns appear due to the selection of some modes. A similar situation is observed in numerical solutions of equations (2). Thus it seems that the steady state structures are not affected by the microscopic fluctuations at least inside the Turing space associated to the rate equations (2) (RETS).

Indeed Turing patterns are also obtained in the CA model for parameters lying outside the RETS. Thus this space is extended by the presence of fluctuations.

An other interesting effect of the fluctuations arises in the study of the short time behaviour of the system. The linearization of the equations (2) around an unstable homogeneous steady state shows an exponential temporal growth of some modes of wavenumber $\vec{l}$, providing that $\vec{l}_1^2 < \vec{l}^2 < \vec{l}_2^2$. Two new features appear in the CA model. First, the window $[\vec{l}_1^2, \vec{l}_2^2]$ becomes larger and secondly the modes in the CA model do not have an exponential growth. This can be explained by the presence of fluctuations which introduce indirectly strong couplings among the modes.

In conclusion, our model is well suited to describe reaction-diffusion systems involving microscopic fluctuations and exhibiting Turing structures. Numerous aspects of the effects of fluctuations on such systems are under investigations[1].

References

[1] M. Droz and L. Frachebourg, to be published.

[2] V. Castets, E. Dulos, J. Boissonade and P. De Kepper, Phys. Rev. Lett. **64** 2953 (90); Q. Ouyang and H. L. Swinney, Nature **352** 610 (91).

[3] A. M. Turing, Philos. Trans. R. Soc. Lond. **B327** 37 (52).

Self-Organized Criticality in the Weakly Driven Frenkel-Kontorova Model[1]

F.J. Elmer

Physics Institute, University of Basel, 4056 Basel, Switzerland

The weakly driven Frenkel-Kontorova model with damping is studied numerically. The dynamics is characterized by random occurrence of reconfiguration events of every size. The probability density as a function of the event strength decays algebraically.

Weakly driven dissipative systems with many metastable states may show a kind of chaotic behaviour called self-organized criticality (SOC) [1]. The key signature of SOC is a random sequence of events with a power-law distribution of the event strengths. In this paper we investigate numerically the dynamics of a linear harmonic chain in an external spatially periodic potential (Frenkel-Kontorova model) with dissipation due to a velocity-proportional friction:

$$\ddot{x}_i + g\,\dot{x}_i + \partial V/\partial x_i = 0, \quad i = 1, \cdots, N, \tag{1}$$

with the potential V

$$V = \sum_{i=1}^{N} \frac{1}{2}(x_i - x_{i-1} - a)^2 - b\cos x_i, \tag{2}$$

where x_i is the position of the ith particle, x_0 is the position of a wall at which the left end of the chain is fixed (the right end can move freely), g is the damping constant, a is the equilibrium length of the springs, and b the strength of the external potential. The stationary states of the Frenkel-Kontorova model may be generated by the well-known Standard or Chirikov map [2]. It is believed that the number of metastable states increases exponentially with the number of particles if b is large enough.

We drive the Frenkel-Kontorova model weakly by moving very slowly the wall at which the chain is fixed, i.e.

$$x_0 = v\,t, \quad \text{with} \quad |v| \ll 1. \tag{3}$$

This leads to well-separated reconstruction events of the chain. Each event corresponds to a saddle-node bifurcation[2] for a certain value of x_0. During an event the kinetic energy E_{kin} increases very rapidly, reaches a maximum and decreases exponentially (i.e. $E_{kin} \propto e^{-\lambda t}$ with $\lambda \approx g$). In the simulation the begin and the end of an event is defined by $E_{kin} = E_1$ (here: $E_1 = 10^{-5}$) and $E_{kin} = E_2 < E_1$ (here: $E_2 = 10^{-6}$), respectively. Define the strength S of an event to be $S = \sum_{i=1}^{N} \delta x_i$, where δx_i is the displacement of the ith particle. Let $p(S)dS$ be the probability of an event whose strength lies between S and $S + dS$. A signature of SOC is $p(S) \cong A/S^{\rho}$, where A and ρ are positive constants. Simulations for various

---

[1] This work was supported by the Swiss National Science Foundation.

[2] Since the Standard map is invertible, x_0 is a function of x_N. The saddle-node bifurcations correspond to extrema of $x_0(x_N)$.

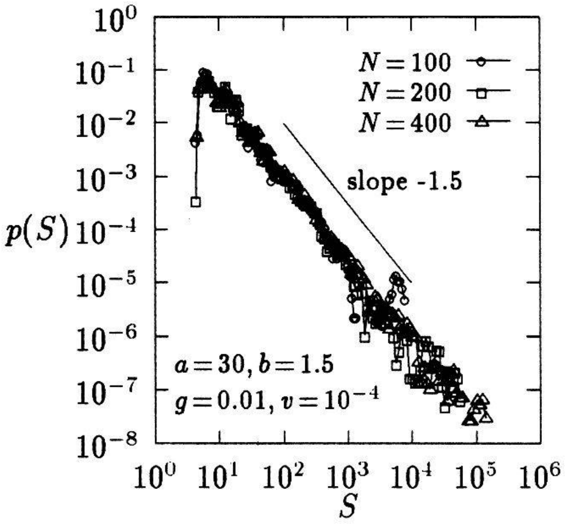

Figure 1: Probability density of three simulations with 1720, 2686, and 2316 events for N = 100, 200, and 400, respectively.

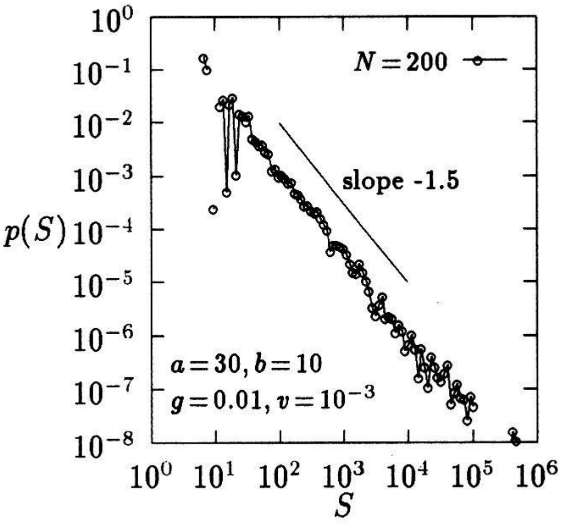

Figure 2: Probability density of a simulation with 2081 events.

values of N and b exhibit clearly SOC with $\rho \cong 1.5$ (see Fig. 1 and 2). For increasing damping constant g, SOC gives place to regular behaviour of well-defined event sequences which reappear periodically. There exist several cycles with different periodicities for the same parameters. SOC also disappears if either the number of particles N or the strength of the external potential b is decreased. This may be caused by the decrease of the number of metastable states. The overall behaviour does not change if the harmonic interaction between the particles is replaced by a Toda-like potential (i.e. $V_{int} = A\,e^{-x} + x$) [3].

References

[1] P. Bak, C. Tang, and K. Wiesenfeld, Phys. Rev. Lett. **59**, 381 (1987); Phys. Rev. A **38**, 364 (1988).

[2] S. Aubry, in *Solitons in Condensed Matter Physics*, edited by A.R. Bishop and T. Schneider (Springer Verlag, New-York, 1978).

[3] F.J.Elmer, Europhysics Letters (1992) in press.

Monte Carlo Study on the CM2 of the Field-induced Interface in the Two-dimensional Ising Model

A. Canning and M. Robert*

Department of Theoretical Physics, University of Geneva,
24 Quai Ernest-Ansermet, CH-1211 Geneva, Switzerland.

* on leave from the Rice Quantum Institute, Rice University,
Houston, Texas 77251-1892, USA.

The structure of the interface between coexisting phases in the two-dimensional Ising model in the presence of a spatially nonuniform external field is studied with Monte Carlo simulation techniques on the CM2. The magnetization profile and the two-point correlation functions are obtained for a step-like external field.

Recent theoretical studies [1] have revealed that the interface between coexisting phases in two dimensions has unexpected remarkable features. In particular, it was discovered [1] that the fundamental idea that the thickness of the critical interface is proportional to the bulk correlation length is incorrect in two dimensions. While this result is believed to be exact [2], a rigorous proof is lacking and in fact appears difficult.

It is well known that at the thermodynamic limit of an infinite system, the interface of two-dimensional systems with short-ranged interactions is rough at all positive temperatures [3], i.e., the order parameter does not vary on the scale of the interactions, unless a spatially nonuniform macroscopic external field is imposed. Unfortunately, unlike the case of one-dimensional systems [4], the exact solution of a two-dimensional model in a nonuniform external field is presently out of reach (even the case of a uniform external field remains unsolved), and it is thus natural to turn to experiment, be it real or simulated on a computer.

Here, we turn to the latter and consider the two-dimensional Ising model with nearest-neighbour interactions on a large square lattice of 512 × 512 spins. Periodic boundary conditions are imposed in both directions and a macroscopic step-like external field is applied. The finiteness of the system itself, independently of the external field, clearly yields an interface of finite thickness. The external field is imposed not only to mimic the theoretical conditions of [1], but also to avoid the spurious slow asymptotic decay of the correlation functions induced by the lack of clustering associated to the rough interface of the infinite field-free system [3].

Our initial goal of studying the critical region has proved more difficult than expected and the first studies described here deal with the structure of the interface away from the critical point. In particular, we wish to compare the asymptotic decay of the correlation function in the interface to that of the correlation function in the bulk, and to compare the behaviour of lattice models with that of continuous ones, in order to test the idea that the slow decay of the correlations in the interface, which is due to low-lying excitations of the "Goldstone type", is not present in lattice models.

Simulations were performed on the Connection Machine CM2 at Geneva University, which is a parallel machine having 8192 processors. The Metropolis algorithm [5] was used

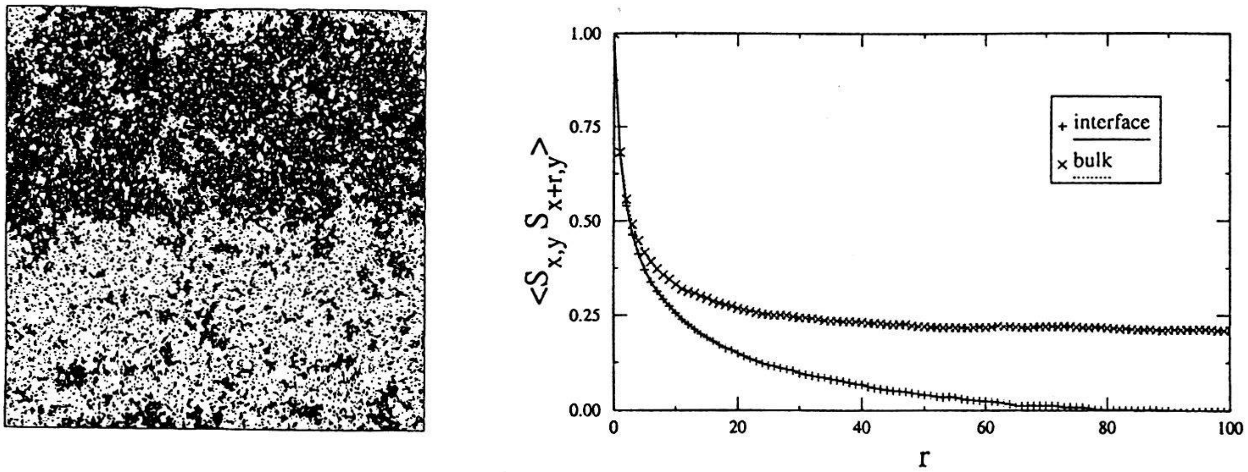

Figure 1: Interface for a 512 × 512 spin system at $\beta(=\frac{1}{k_BT}) = 0.435$ ($\beta_c = 0.44068$) with an external field $h = 0.001$ on the upper half and $h = -0.001$ on the lower half. The spin directions up and down are represented by black and white respectively. The graph shows the two-point correlation function $< S_{x,y}S_{x+r,y} >$ measured along the center of the interface and in the bulk at the furthest distance from the interface ($\beta = 0.435, h = 0.0005$).

to generate numerically the Gibbs distribution for our model. This algorithm suffers from critical slowing down close to T_c, but since our simulations were performed above T_c and on a parallel machine, it was well suited for our purposes. Mapping the problem onto the CM2 it was possible to update 8192 spins in parallel and obtain from 20 to 100 million spin updates per second, depending on the system size and algorithm.

A typical equilibrium distribution is shown in the left figure. The graph to the right shows the two-point correlation function $< S_{x,y}S_{x+r,y} >$ measured along the center of the interface and in the bulk. Above T_c with $h = 0$ and for large r the two-point correlation function of the bulk phase is proportional to $r^{-\frac{1}{2}} \exp\frac{-r}{\xi}$, where ξ is the correlation length. Our initial numerical results for small field and large r fit well to this functional form for the bulk while the correlation function for the interface appears to be exponential but factored by a different power of r. This suggests that there are no excitations of the "Goldstone type". The correlation length also appears to be larger for the interface than for the bulk. More detailed studies of the two-point correlation function as a function of T and h will be presented elsewhere.

This work was partly supported by the Welch Foundation (Houston, USA) and the Physics Department at Geneva University. M.R. is grateful to the latter for its hospitality.

References

[1] M.Robert, *Phys. Rev.* **A30**, 2785 (1984).
M.Knackstedt and M.Robert, *Int. J. Thermophys.*, **10**, 321 (1989).

[2] M.P.Gelfand and M.E.Fisher, *Physica*, **A166** 1, 20 (1990).

[3] G.Gallavotti, *Commun. Math. Phys.*, **27**, 103 (1972).

[4] M.Robert and R.Viswanathan, *J. Chem. Phys.*, **86**, 4657 (1987).

[5] K.Binder and D.W.Heermann, Monte Carlo Simulation in Statistical Physics, Springer-Verlag, (1988).

Why Does Linear Response Theory Work in Systems with Highly Nonlinear Dynamics

W. Breymann

Institut für Physik, Klingelbergstr. 82, 4056 Basel, Switzerland

The van Kampen problem for linear response theory is discussed by means of a simple model that can be treated analytically.

In spite of the success of linear response theory, there is still some criticism on its derivation [1]. Indeed, taking the equivalence of time average and ensemble average for granted, the susceptibility for an observable B is given by $\int d\Gamma B\, d(\hat{\rho}_\alpha(t))/d\alpha$, where $\hat{\rho}_\alpha(t)$ signifies the perturbed density at time t. Since time dependence can be transferred from the density to the observable, this expression is equivalent to $\int d\Gamma \rho_0^*\, d\hat{B}_\alpha(t)/d\alpha$, i.e., to an average of the linearization in the perturbation α of the individual trajectories $\hat{B}_\alpha$ over the unperturbed invariant density ρ_0^*. Van Kampen [1] raised the question which mechanism will assure that the linear approximation remains valid for the density even though it breaks down for the trajectories at values of α which tend to zero for infinite times.

In the present note, some elements to the answer are presented by demonstrating for a specific case why the response remains smooth. As in ref. [2],

$$f_0 : \begin{pmatrix} x \\ y \end{pmatrix} \mapsto \begin{pmatrix} 1 & 1 \\ 1 & 2 \end{pmatrix} \begin{pmatrix} x \\ y \end{pmatrix} \bmod 1\,, \tag{1}$$

the so-called cat map, has been taken for the unperturbed system. It is completely chaotic and has a positive Lyapunov exponent $\lambda \approx 0.962$. For sufficiently small α, the perturbed map can always be obtained by conjugation with an appropriate perturbative function g_α: $\hat{f}_\alpha = \hat{g}_\alpha^{-1} \circ f_0 \circ \hat{g}_\alpha$ [3] where $g_0 = id$. For the specific choices of the perturbation and the observable, we again refer to ref. [2]. These choices have the advantage to be analytically treatable. The perturbation acts only on the x-coordinate: $[g_\alpha]_y(x,y) = y$, and

$$[g_\alpha]_x(x,y) = \begin{cases} (1+2\alpha)x & \text{if} \quad x < 1/2 \\ (1-2\alpha)x - 2\alpha & \text{if} \quad x > 1/2. \end{cases} \tag{2}$$

For the observable $B(x,y) = x$, the response of an individual orbit is given by $\hat{x}_\alpha(x_0, y_0, t) = [g_\alpha^{-1}]_x(f^t(g_\alpha(x_0,y_0)))$. In Fig. 1, $\hat{x}_\alpha$ is shown as a function of α for some initial condition (x_0, y_0) and for $t = 4$ and $t = 6$. The overall sawtooth-like shape of this function is determined by the stretching and folding process of the map: one tooth corresponds to one fold. The slope of the ascending (left) side of a fold is due to stretching and proportional to $e^{\lambda t}$, whereas the features of the descending side are governed by the folding which takes place instantaneously. The linear approximation is valid only within the limits of one fold, i.e., for a range proportional to $e^{-\lambda t}$. The α-values at which folding occurs depend on x_0 and y_0.

In order to evaluate the full mean response, the ensemble average with respect to ρ_0^*,

$$\langle \hat{x}_\alpha(t) \rangle_{\rho_0^*} = \int_0^1 dy_0 \int_0^1 dx_0\, [g_\alpha^{-1}]_x(f^t(g_\alpha(x_0,y_0))), \tag{3}$$

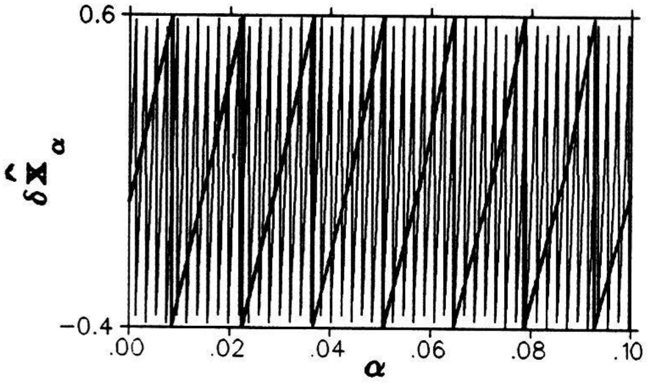

Fig. 1: $\delta\hat{x}_\alpha(x_0, y_0, t) = \hat{x}_\alpha(x_0, y_0, t) - x(x_0, y_0, t)$ as function of α for $(x_0, y_0) = (0.4, 0.2)$. $t = 6$ (bold), $t = 8$ (normal line).

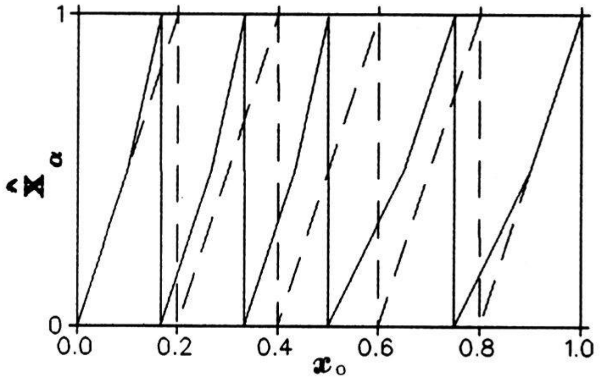

Fig. 2: $\hat{x}_\alpha(x_0, y_0, t)$ as function of x_0 for $y_0 = 0.5$ and $t = 3$. $\alpha = 0$ (broken), $\alpha = 0.1$ (normal line).

has to be calculated for fixed α and t. The x_0-dependence of the integrand is plotted in Fig. 2 for $\alpha = 0$ and $\alpha = 0.1$. In both cases, the function displays regularly repeating folds the number $N(t)$ of which remains constant under perturbation. For $\alpha = 0$, the folds are regular triangles with base length $1/N(t)$ and area $1/(2N(t))$. Eq. (3) can thus be evaluated trivially. There is a one-to-one correspondence between the folds of the unperturbed and the perturbed case, but in the latter, they are distorted. Their area evaluates to $(1-\alpha)/(2(1+2\alpha)N)$ and $(1-\alpha)/(2(1-2\alpha)N)$ for $x_0 < 1/2$ and $x_0 > 1/2$, respectively. Even though the number of folds increases with t, what counts for the validity of the linear response is the relative change of the area of a fold with respect to the corresponding non-disturbed one. This changement is given by $(1-\alpha)/(1+2\alpha)$ and $(1-\alpha)/(1-2\alpha)$, respectively. It is thus smooth in α and independent of t even for large values of α, and at $\alpha = 0$, the slope of the mean value happens to coincide with the average of the initial slopes of the trajectories at the same time t. Consequently, the range of validity of the linear approximation of the averaged response does not depend on t.

For this result to be valid, the general features of the system are that (i) the stretching and folding process should not change under perturbation and (ii) the class $\{g_\alpha\}$ of perturbative functions should be smooth (or at least continuous) in α for fixed (x_0, y_0). The first condition is fulfilled for so-called C-systems [3], while (ii) should be satisfied for all physically reasonable perturbations. In spite of the fact that a very specific example has been treated here, the author believes that the result will hold, at least qualitatively, for other systems that meet these requirements.

The author thanks H. Thomas for fruitful discussions and valuable comments. The financial support of the Swiss National Science Foundation is gratefully acknowledged.

References

[1] N. G. van Kampen, Physica Norvegica **5**, 279 (1971); unpublished (1976).

[2] W. Breymann and H. Thomas, *in* G. Györgyi et al. [eds.], *from Phase Transitions to Chaos* (World Scientific, Singapore, 1992).

[3] V. I. Arnold , *Geometrische Methoden in der Theorie der gewöhnlichen Differentialgleichungen,* Sec. 3.4 (Birkhäuser, Basel, 1987).